REVIEW

NANO · MICRO small

www.small-journal.com

Exceedingly Small Magnetic Iron Oxide Nanoparticles for T_1-Weighted Magnetic Resonance Imaging and Imaging-Guided Therapy of Tumors

Jing Yang, Jie Feng, Sugeun Yang, Yikai Xu,* and Zheyu Shen**

Magnetic iron oxide nanoparticles (MIONs) based T_2-weighted magnetic resonance imaging (MRI) contrast agents (CAs) are liver-specific with good biocompatibility, but have been withdrawn from the market and replaced with Eovist (Gd-EOB-DTPA) due to their inherent limitations (e.g., susceptibility to artifacts, high magnetic moment, dark signals, long processing time of T_2 imaging, and long waiting time for patients after administration). Without the disadvantages of Gd-chelates and MIONs, the recently emerging exceedingly small MIONs (ES-MIONs) (<5 nm) are promising T_1 CAs for MRI. However, there are rare review articles focusing on ES-MIONs for T_1-weighted MRI. Herein, the recent progress of ES-MIONs, including synthesis methods (the current basic synthesis methods and improved methods), surface modifications (artificial polymers, natural polymers, zwitterions, and functional protein), T_1-MRI visual strategies (structural remodeling, reversible self-assemblies, metal ions doped, T_1/T_2 dual imaging modes, and PET/MRI strategy), and imaging-guided cancer therapy (chemotherapy, gene therapy, ferroptosis therapy, photothermal therapy, photodymatic therapy, radiotherapy, immuotherapy, sonodynamic therapy, and multimode therapy), is summarized. The detailed description of synthesis methods and applications of ES-MIONs in this review is anticipated to attract extensive interest from researchers in different fields and promote their participation in the establishment of ES-MIONs based nanoplatforms for tumor theranostics.

1. Introduction

The importance of early and accurate tumor diagnosis has received widespread acclaim for saving cancer patients' lives.[1] Currently, the advanced imaging techniques that can be utilized for tumor diagnosis include magnetic resonance imaging (MRI), computed tomography (CT), and positron-emission tomography (PET).[2] Among these imaging techniques, MRI is a popular one due to its broad clinical applicability, high spatial resolution, high contrast for soft tissues, unlimited signal penetration depth, and no ionizing radiation.[3] MRI relies upon the exquisite detection of nuclear magnetic resonance signals emanating from hydrogen protons in vivo. The MRI signals could be dramatically strengthened by contrast agents (CAs).[4]

The improvement in MRI contrast is due to the CAs interacting with the protons of the water, which speeds up the longitudinal (T_1) and/or transverse (T_2) relaxation time of the water in the surrounding environment.[5] In general, the utilization of T_1-weighted contrast agents can augment the signal intensity, thereby eliciting a favorable enhancement in contrast. On the contrary, T_2-weighted CAs are utilized to decrease the signal intensity, resulting in a negative contrast improvement. The longitudinal relaxivity (r_1) or transverse relaxivity (r_2) is respectively defined as the slope from a plot of CAs concentration versus longitudinal relaxation rate ($1/T_1$) or transversal relaxation rate ($1/T_2$). The r_1 value, r_2 value, and r_2/r_1 ratio are commonly used to assess the effectiveness of MRI CAs. The higher r_1 value and lower r_2/r_1 ratio of T_1-weighted CAs lead to stronger T_1-MRI efficiency. In addition, higher r_2 value and higher r_2/r_1 ratio of T_2-weighted CAs result in stronger T_2-MRI efficiency.[6]

Magnetic iron oxide nanoparticles (MIONs) have been extensively researched in laboratories, reported in literatures, and clinically transformed as T_2-weighted CAs, including Endorem (from Guerbet, France), Feridex (from Berlex, USA), Resovist (Schering AG, Germany), and so on.[7] Feridex and Endorem are colloids of MIONs, which are coated with dextran. The whole particle size is 120–180 nm, and the r_1 and r_2 values are respectively ≈24 and ≈98 $\text{mM}^{-1}\ \text{s}^{-1}$. Resovist is also a colloid of MIONs and coated by

J. Yang, Z. Shen
School of Biomedical Engineering
Southern Medical University
1023 Shatai South Road, Baiyun, Guangzhou, Guangdong 510515, China
E-mail: sz@smu.edu.cn

J. Feng, Y. Xu
Medical Imaging Center
Nanfang Hospital
Southern Medical University
1023 Shatai South Road, Baiyun, Guangzhou, Guangdong 510515, China
E-mail: fjnfyy@smu.edu.cn; yikai@smu.edu.cn

S. Yang
Department of Biomedical Science
BK21 FOUR Program in Biomedical Science and Engineering
Inha University College of Medicine
Incheon 22212, South Korea

The ORCID identification number(s) for the author(s) of this article can be found under https://doi.org/10.1002/smll.202302856

DOI: 10.1002/smll.202302856

carboxydextrane, whose whole particle size is 45–60 nm, much smaller than Feridex and Endorem. The r_1 and r_2 values are respectively ≈25 and ≈150 mM^{-1} s^{-1}.

The MIONs-based T_2 CAs have good biocompatibility because they could be metabolized to not-toxic iron ions in vivo. However, most of the commercialized MIONs-based T_2 CAs have been withdrawn from the market due to the following reasons. 1) The dark signals resulted from the T_2 CAs are hard to be distinguished by the naked eyes, and are similar to some pathogenic conditions, such as hemorrhage, calcification, and metal deposits.[8,9] 2) The magnetic moments of T_2 CAs are high, which can result in the magnetic field distortion around disease areas (i.e., susceptibility artifact).[10] 3) The particles sizes of MIONs-based T_2 CAs are immense, ranging from 45 to 180 nm, which needs a long time to achieve maximum accumulation of the particles in disease regions, e.g., tumors, and then results in a lengthy waiting period for patients after administration of the CAs. 4) The extended echo time (TE) and repetition time (TR) contribute to an elongated processing duration for T_2 imaging, consequently placing a greater demand on MRI machines in clinical settings. 5) Due to the above four reasons, the MIONs-based T_2 CAs are almost only utilized for liver disease due to their liver-specificity. A liver-specific T_1 CA Eovist (i.e., Gd-EOB-DTPA) that was approved in 2008 made them completely useless.

Because of the above-mentioned drawbacks of T_2 CAs, T_1 CAs are most commonly used in the clinic, and future developments of MRI CAs will be probably focused on T_1 CAs.[11,12] Remarkably, the highly minute MIONs (ES-MIONs) have garnered extensive research attention as T_1 contrast agents, owing to their remarkable biocompatibility, with a size that is less than 5 nm.[13–15] Although several review articles have been published focusing on iron oxide-based nanoparticles,[16] magnetic nanoparticles,[17] or inorganic nanoparticles[18] as MRI CAs and tumor therapeutic agent, up to now, rare review article focusing on ES-MIONs for T_1-MRI has been reported in the literature.

In this review, we concentrate on the ES-MIONs including their synthesis methods, surface modification strategies, T_1-MRI tumor imaging and T_1-MRI imaging-guided cancer therapy, as shown in **Figure 1**. Finally, we give a future perspective of ES-MIONs for cancer theranostics, including the challenges and opportunities.

2. T_1-Weighted MRI CAs

The current T_1 MRI CAs mainly include Mn-chelates, Gd-chelates, and magnetic nanoparticles.

2.1. Mn-Chelates

Mn is an important biological metal in most tissues (average concentration in serum is 0.5–1.2 µg L^{-1}). It is crucial to bone development, neuronal health physiological reaction, and other cellular functions. The application of Mn^{2+} ions as T_1 contrast agents stems from their possession of five unpaired electrons, resulting in a protracted electronic relaxation period.[19,20] The proton spins interaction with Mn^{2+} ions is considered as the primary dipolar interaction accountable for their relaxation properties, which contributes to a high T_1 signal enhancement. Up to now, mangafodipir trisodium (Mn-DPDP) have been a commercial MRI contrast agents on the market.[21] Mn-DPDP (manganese chelate) is created as an MRI contrast agent for hepatobiliary system. DPDP is a biological coordination group, which is usually recognized by the membrane transport system of pyridoxal phosphate (PLP). The lethal dose of Mn-DPDP is nearly 18-fold higher than that of MnCl$_2$, and the chelation also leads to partial excretion of manganese through the kidney.[22] Consequently, a great interest has been attracted in the creation of next generation Mn CAs, with 1) higher r_1 and lower r_2/r_1; 2) high thermodynamic stability; 3) stability at physiological conditions; 4) fast clearance in vivo.[23,24]

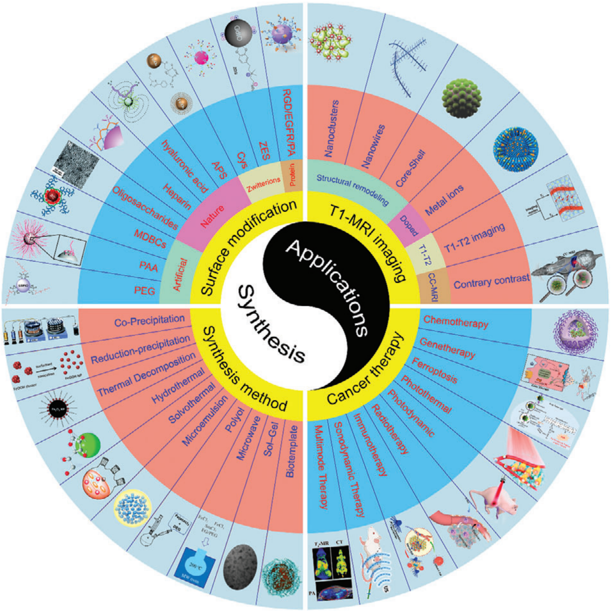

Figure 1. A schematic illustration of ES-MIONs including synthesis methods, surface modification, T_1-MRI strategies, and MRI-guided cancer therapy.

2.2. Gd-Chelates

The commercial Gd-chelates have accounted for the majority of the MRI CAs market for decades, including Omniscan (Gd-DTPA-BMA), Dotarem (Gd-DTOA), OptiMARK (Gd-DTPA-BMEA), Magnevist (Gd-DTPA), Eovist (Gd-EOB-DTPA), Gadovist (Gd-DO3A-Butriol), Multihance (Gd-BOPTA), and ProHance (Gd-HP-DO3A).

The advantages of Gd-chelates include: 1) they only need a short time (<20 min) to achieve maximum accumulation in disease regions, which results in a short waiting time for patients; 2) their r_2/r_1 ratios are very low (<1.1 at 1.5 T of magnetic field), which benefits T_1-weighted MRI; 3) They are quickly excreted from the body via renal excretion. However, there are still several unsolved problems for Gd-chelates, which impede their clinical applications. 1) The Food and Drug Administration (FDA) of the United States has issued a comprehensive cautionary notice regarding their clinical implementation due to their potential nephrotoxic properties.[25,26] or deposition in brain.[27] 2) Their r_1 values are low (only ≈4 mM^{-1} s^{-1} at 1.5 T), which

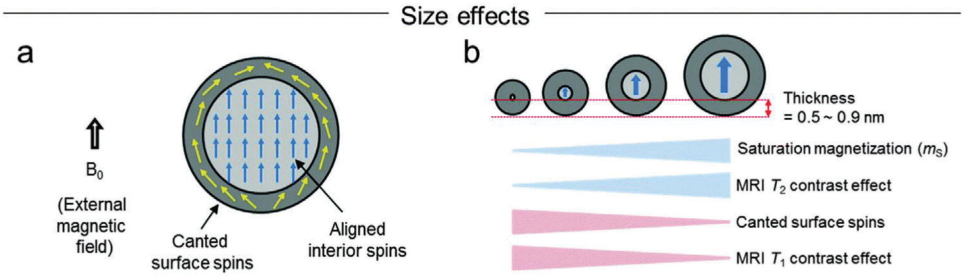

Figure 2. The effects of magnetic nanoparticles on enhancing MRI contrast.[28] A) Alignment of magnetic spins (including interior and surface spins) of nanoparticles under an external magnetic field (B0). B) Magnetic nanoparticle size versus ms, T_2 contrast effects, canted surface spins, and T_1 contrast effects. Reproduced with permission.[28] Copyright 2015, Royal Society of Chemistry.

is not good for T_1 imaging. 3) The majority of them are neither tissue- or cell-specific. Because of these disadvantages, the Gd-chelates may no longer be produced and used in the future. Thus, the magnetic nanoparticles served as T_1 CAs have emerged the enormous potential to replace the commercial Mn- and Gd-chelates.

2.3. Magnetic Nanoparticles

Magnetic nanoparticles can be applied as valid T_1 CAs because their r_1, r_2, and r_2/r_1 can be easily regulated by nanoparticle magnetism optimization. In T_1-weighted nanoparticles, the T_1 contrast effect is derived from the presence of a magnetically disordered spin layer on the surface of the magnetic nanoparticles (**Figure 2**).[28] The metal ions residing on the surface of magnetic nanoparticles exhibit diverse quantities of unpaired electrons, exerting a substantial influence on the T_1 relaxation process. The high r_2 and r_2/r_1 values caused by nanoparticles magnetization are not suitable for T_1 CAs. The saturation magnetization (Ms) of nanoparticles escalates as the dimensions of the magnetic nanoparticles expand, as depicted in Equation (1).

$$M_s = M_s[1 - d/r]^3 \tag{1}$$

wherein, “r” denotes the nanoparticle radius, and “d” represents the thickness of the disordered surface spin layer. Thus, a strategic approach to achieve elevated r_1 values and diminished r_2 values is to augment the proportion of canted surface spins in the nanoparticles. Theoretical investigations suggest that a substantial T_1 contrast effect can be attained when the magnetic nanoparticles are smaller than 5 nm in size. The T_1 CAs of magnetic nanoparticles include Gd-based nanoparticles, Mn-based nanoparticles, and ES-MIONs. Their classification, advantages, and limitations are discussed and clarified as follows.

2.3.1. Gd-Based Nanoparticles

Compared with the commercial Gd-chelates, Gd-based nanoparticles exhibit excellent T_1 MRI efficiency with extended blood circulation time and well biocompatibility. Furthermore, the Gd-based nanoparticles can be modified with chemical reagent, targeting ligands, and fluorescence dyes to form a multifunctional nanoplatform to support multimodal imaging and remedy.[29] For example, Gd-based nanoparticles, including Gd_2O_3, $RbGdF_4$, $NaGdF_4$, and $Gd_{0.74}Eu_{1.26}O_3$, have been widely studied for their T_1-Weighted MRI.[30] In addition, Gd-based nanoparticles can also be applied as multifunctional imaging, including T_1-weighted MR, UCL (upconversion luminescence), and CT imaging.[31]

Shen et al. synthesized ES-GON-PAA using wet-chemical synthesis method utilizing a stabilizer of PAA. The ES-GON5-PAA nanoparticles obtained at the optimized synthesis conditions have extraordinary relaxivities with 70.2 ± 1.8 mM^{-1} s^{-1} of r_1 and 1.02 ± 0.03 of r_2/r_1 at 1.5 T. Both r_1 and r_2/r_1 are significantly superior to the previously reported GONs and commercial Gd chelates.[32,33] Further, Shen et al. synthesized novel organogadolinium complex nanoparticles via reaction of $GdCl_3$, reductive bovine serum albumin (rBSA), and sodium salicylate (NaSal) in aqueous solutions. The resulting nanoparticles exhibit excellent water-dispersibility, displaying a remarkable r_1 value of 19.51 mM^{-1} s^{-1} and a favorable r_2/r_1 ratio of 1.21 (1.5 T). These properties make it highly suitable for high-contrast T_1-MRI imaging of tumors.[34]

Despite the fact that Gd-based nanoparticles show tremendous promise in clinical applications, their limitations are frequently cited, including water dispersibility, possible Gd release, and unpredictable renal toxicity.

2.3.2. Mn-Based Nanoparticles

Manganese oxide nanoparticles are another kind of promising candidates for T_1 CAs. Mn-based nanoparticles, including MnO NPs,[35] Mn_3O_4 NPs,[36] and MnO_2 nanosheets,[37] have been developed as T_1 CAs due to their regulated manganese ions release at acidic conditions, and easily changeable valency.[35] Pan et al. fabricated biocompatible MnO_2 nanoparticles encapsulated in BSA with a size of merely 3 nm. These nanoparticles exhibit a favorable T_1 signal with an r_1 value of 5.9 mM^{-1} s^{-1}, alongside excellent biocompatibility.The BSA-MnO_2 nanoparticles are used for the noninvasive and timely visualization of blood-brain barrier permeability in the model rats.[38] To be used clinically, the following 4 aspects of the Mn-based nanoparticles should be improved: 1) higher r_1 and lower r_2/r_1; 2) smaller particle size for renal excretion; and 3) better water dispersibility.

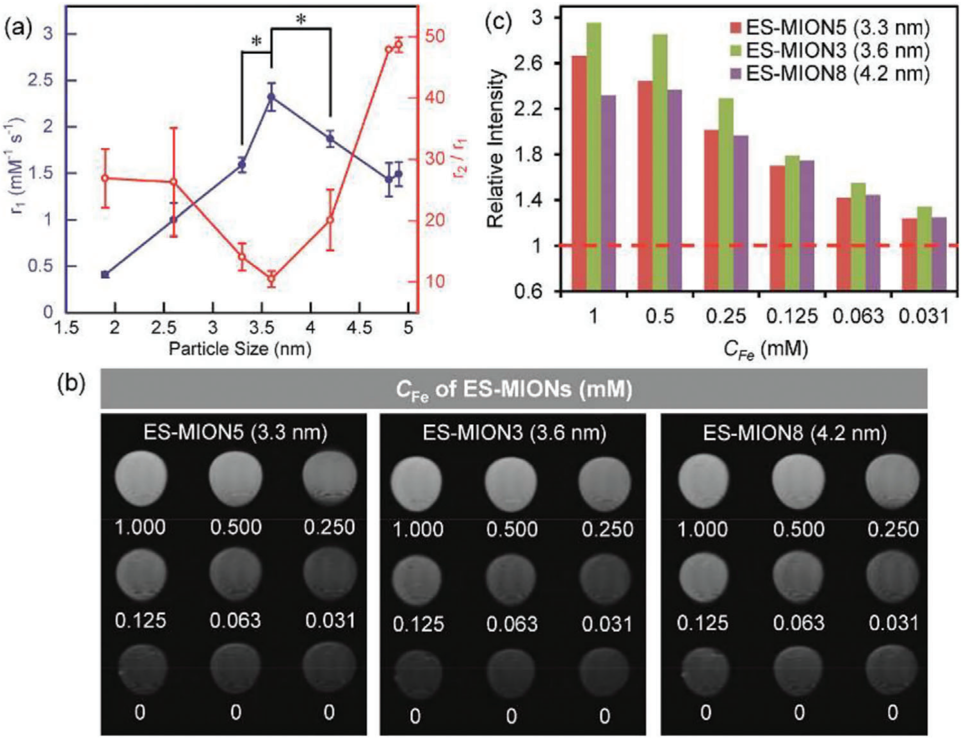

Figure 3. MRI efficiencies of the ES-MIONs. A) r_1 value and r_2/r_1 ratio of ES-MIONs with different diameter size. B) T_1-weighted MR images of ES-MION at various Fe concentrations at 7.0 T. C) Relative intensity of the MR images for ES-MIONs. Reproduced with permission.[105] Copyright 2017, American Chemical Society.

2.3.3. ES-MIONs

Iron oxide nanoparticles are considered to possess greater biocompatibility compared to Gd-based or Mn-based nanoparticles. This is due to the presence of iron in human blood, primarily held within ferritin.[39] Although Fe^{3+} has five unpaired electrons to increase the r_1, the high r_2 of MIONs due to the high magnetic moment inhibits the T_1 efficiency.

It has been shown that small-sized MIONs with a diameter below 5 nm can be utilized as T_1 CAs. As the particle size of MIONs decreases, the coupled magnetic moment experiences a rapid decline, conferring substantial advantages in impeding the T_2 contrast effect and ultimately optimizing the T_1 effect. Shen et al. precisely controlled the size of ES-MIONs to be 1.9, 2.6, 3.3, 3.6, 4.2, 4.8, and 4.9 nm, and found that 3.6 nm of ES-MIONs has the best T_1 contrast efficiency. With the particle size increase in range of 1.9-3.6 nm, the r_1 increases and the r_2/r_1 decreases. However, in the range of 3.6-4.9 nm, with an increase in particle size, the r_1 declines and the r_2/r_1 rises. (**Figure 3**).[15] The r_1 value of iron oxide nanoparticles can be affected by a number of variables. On the one hand, bigger particles have greater saturation magnetization (Ms), which causes stronger interactions between Fe and nearby diffusing water molecules without interacting with Fe (the outer sphere), resulting in larger r_1 values (i.e., the outer-sphere model). As a result, the r_1 value rose as the size of the ES-MIONs grew from 1.9 to 3.6 nm. On the other hand, bigger nanoparticles have lower specific surface areas, which leads to less bare Fe on the nanoparticle surface that directly interacts with water molecule hydrogen nuclei (the inner sphere), resulting in a reduced r_1 value (i.e., the inner-sphere model).

The blood circulation half-time ($t_{1/2}$) has been summarized in the **Table 1**. As the exceedingly small size of ES-MIONs, it shows a short blood circulation half-time at ≈2 h. The time frame for MRI in a clinic is close to the half-life (10-15 min) of commercial Gd chelates, making MRI following Gd chelate administration a little tight. The somewhat longer half-life of ES-MIONs solves the difficulty of commercial Gd chelates' narrow MRI time frame. Furthermore, ES-MIONs accumulate in tumors at a much higher rate than in other normal tissues owing to the increased permeability and retention (EPR) effect.[40] Therefore, ES-MIONs with high hydrophilicity and tumor accumulation property have been widely developing as T_1 contrast agents.

3. Synthesis of ES-MIONs

Because the size and morphology initially determine the properties of ES-MIONs, the selection of a suitable synthesis method is essential. Generally, the control of the nucleation and growth process is very important for synthesizing monodisperse ES-MIONs. Various synthesis strategies generate ES-MIONs with different surface properties, morphologies, sizes, and crystallinity. Typical reported synthesis methods include co-precipitation, reduction-precipitation, thermal decomposition, hydrothermal, solvothermal, microemulsion, polyol, microwave, sol-gel, and biotemplate methods. Herein, we introduce and

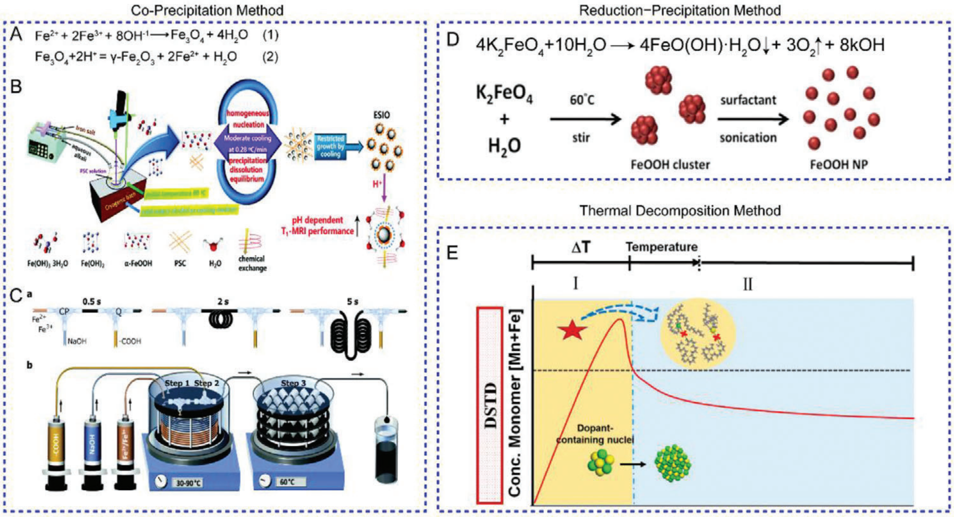

Figure 4. Primary synthesis methods for ES-MIONs. A) The co-precipitation method mechanism of chemical reaction for Fe_3O_4 and γ-Fe_2O_3. B) A method utilizing mild cooling coprecipitation for synthesizing ES-MIONs. Reproduced with permission.[52] Copyright 2020, Royal Society of Chemistry. C) Multistage flow reactor initiated co-precipitation, quenching, and stabilization and aging. Reproduced with permission.[53] Copyright 2021, Royal Society of Chemistry. D) FeOOH NPs preparetion process. Reproduced with permission.[54] Copyright 2013, American Chemical Society. E) Mechanism for DSTD synthesis of manganese ferrite nanoparticles. Reproduced with permission.[46] Copyright 2017, American Chemical Society.

discuss the advances of ES-MIONs synthesis using the above-mentioned methods.

3.1. Co-Precipitation Method

During the co-precipitation process, iron ions (Fe^{2+} and Fe^{3+}) are concomitantly precipitated into iron oxides through the utilization of a mild alkali reagent such as ammonia, sodium hydroxide, TMAOH, and so forth. The co-precipitation reaction of Equation (1) is shown in **Figure** 4A.[49] In the process of co-precipitation, the morphology, particles size, and dispersion of ES-MIONs depend on the reaction conditions, such as the Fe^{2+}/Fe^{3+} ratio, the reaction system pH value, and the reaction temperature.

In addition, the crystal grain growth inhibitor and stabilizer are also crucial to obtain the uniformity size of ES-MIONs. Wang et al. developed a one-step co-precipitation approach to synthesize the appropriate ES-MIONs with a diameter of 2.2 nm, with poly(acrylic acid) (PAA) acting as the stabilizer and crystal growth inhibitor. The —COOH of PAA have a strong coordination affinity to Fe^{3+} resulting in the growth inhibition of ES-MIONs.[50]

Li et al. synthesized monodispersed ES-MIONs without further modification utilizing a coprecipitation method at high temperature, with thiol-functionalized poly(methacrylic acid) acting as a stabilizer. The ES-MIONs showed a better-controlled size of 3.3 ± 0.5 nm and size distribution because of a burst of nucleation and strong coordination ability of polymer ligands, which lead to the separation between nucleation and growth processes. In addition, the ES-MIONs were used as efficient T_1 and T_2-CAs with larger r_1 and r_2 than those of Gd-DTPA agent.[51]

Nevertheless, the co-precipitation reaction is thermodynamically driven, and the size distribution and crystallinity of the nanopaticles are hard to be controlled. To obtain the uniform size of ES-MIONs, Chen et al., focused on the nucleation and growth stage of co-precipitation reactions (Figure 4B). They presented a moderate cooling preparation strategy to synthesize

Table 1. The summary of the blood circulation half-time ($t_{1/2}$) of ES-MIONs.

Formulation	Diameter	Blood circulation half-time ($t_{1/2}$)	Ref.
ANG/PEG-USPIONs	Hydrodynamic size 14.6 nm	1.71 h	[41]
PA-USPIONs	Hydrodynamic size 13.7 nm	1.84 h	[42]
PEG-functionalized USPIOs	Hydrodynamic size 9.9 nm	2–5 h	[43]
Fe_3O_4-mPEG and Fe_3O_4–PEG–Cys	TEM size 3.1 and 3.2 nm	2.1 and 6.2 h	[44]
FeS@BSA	Hydrodynamic size 11.7 nm	2.12 h	[45]
UMFNPs	TEM size 3 nm	0.31 h	[46]
FGNP@TA-Fe3/Ca4	Hydrodynamic size 16.5 ± 2.2 nm	2.42 h	[47]
poly (aspartic acid) (PASP) coated ES-MIONs	TEM size 3.7 nm	2.3 h	[40]
IONs	TEM size 4.4 nm	2.6 h	[48]

monodispersed ES-MIONs by tuning starting temperature, cooling rate, and so forth.[52]

Ulteriorly, microfluidics technology is used to achieve the uniform size of ES-MIONs. Besenhard et al. prepared the ES-MIONs (≤5 nm) via co-precipitation by terminating particle growth in a microfluidic multistage flow reactor after the magnetic iron oxide phase formed (Figure 4C). The flow-produced ES-MIONs exhibit remarkable T_1 MRI efficacy owing to their elevated r_1 value (>10 mᴍ$^{-1}$ s^{-1}) and diminished r_2 value (20.5 mᴍ$^{-1}$ s^{-1}).[53]

3.2. Reduction–Precipitation Method

Chou et al. reported a reduction-precipitation synthesis of ES-MIONs involving a redox reaction between K_2FeO_4 and water molecules (Figure 4D). First, ferric hydroxide (FeOOH) nanoclusters, with an approximate diameter of 40 nm, are synthesized via redox reactions between potassium ferrate (K_2FeO_4) and water. During sonication, surfactant (citric acid) chelation is employed to disassemble the clusters, which are composed of several crystalline FeOOH particles (≈6 nm), into well-dispersed monodisperse FeOOH nanoparticles. Moreover, the FeOOH nanoparticles exhibit an r_2 value that is two orders of magnitude lower than that of the current ES-MIONs, resulting in the lowest r_2/r_1 ratio.[54]

Furthermore, Chou et al. synthesized glutathione-functionalized ES-MIONs with a diameter of ≈3.7 nm via a reduction-precipitation approach. Tetrakis(hydroxymethyl)-phosphonium chloride (THPC) is applied as a reducing agent to produce ES-MIONs.The prepared ES-MIONs possed a high r_1 (3.63 mm^{-1} s^{-1}) and a minor r_2 (8.28 mm^{-1} s^{-1}) at 4.7 T in cause of the intrinsic antiferromagnetic feature. Thus, owing to the low r_2 value, low r_2/r_1 ratio, and excellent biocompatibility, these ES-MIONs are considered to be an ideal candidate for T_1 CAs.[55]

3.3. Thermal Decomposition Method

Thermal decomposition is conducted under an atmosphere using a mixture of metal precursor (e.g., iron carbonyl $Fe(CO)_5$, iron acetylacetonate $Fe(acac)_3$or), growth inhibitor, reductant, surfactant (e.g., oleic acid, oleylamine, hexadecanediol or octadecylene), and organic solvent with high boiling point (e.g., dioctyl ether or dibenzyl ether) for the synthesis of ES-MIONs. By modifying the kind of solvent, surfactant ratio, and heating strategy (e.g., reaction temperature, reaction duration), the monodisperse ES-MIONs with controlled shape and size can be produced. In the meantime, the thermal decomposition method is a universal approach in monodisperse nanoparticles synthesis. The mixture of precursor and surfactant is heated at a comparatively low temperature, and nanoparticles are formed progressively during the heating process.

Wei et al. synthesized the ES-MIONs via the thermal decomposition method with a mixed solvent designed for tuning boiling point. The ES-MIONs were prepared with an inorganic core and diameters ranging from 2.5 to 7.0 nm by varying the boiling point of solvent solutions including 1-tetra-decene (TDE), 1-hexadecene (HDE), and 1-octadecene (ODE).[56]

Fan et al. reported a general dynamic simultaneous thermal decomposition (DSTD) strategy for the preparation of monodisperse ES-MIONs (Figure 4E). They created Fe-eruciate, a novel kind of coordination complex precursor with a higher dissociation temperature of 326 °C, which is extremely near to Mn-oleate at 311 °C. The synthesis of manganese-doped ES-MIONs involves the amalgamation of mixed iron-eruciate and manganese-oleate complexes, accompanied by the presence of oleic acid and oleyl alcohol, within the confines of benzyl ether or 1-octadecene. By finely tuning the ratio of oleyl alcohol to oleic acid and carefully regulating the reaction temperature, the particle size of the ES-MIONs can be precisely modulated, ranging from a diminutive 2 nm to a more substantial 3.9 nm.[46]

However, due to the high temperature of the synthesis process, the reaction conditions are more rigorous, requiring multi-step operations that are time-consuming, intricate, and inefficient. Furthermore, because of the complicated dynamic nucleation and growth process, thermal degradation of organic precursors remains a difficulty to produce well-controlled size.

3.4. Hydrothermal Method

For the hydrothermal method, the reaction system is particular with a high heating temperature (100–250 °C) and high pressure (0.3–4.0 MPa). The hydrothermal synthesis method bestows an array of advantages, consisting of the exclusion of organometallic compounds and organic solvents, straightforward reaction conditions, exemplary purity, exceptional crystallinity, and remarkable water dispersibility of the ES-MIONs.

Xiao et al. developed a new method to synthesize water-soluble and biocompatible ES-MIONs (size is ≈5.1 nm) by reduction of $Fe(OH)_3$ colloid using a natural reducing agent(vitamin C; **Figure 5**A). During the synthesis process, $Fe(OH)_3/Fe(OH)_2$ colloids were accurately adjusted by the addition of vitamin C. Within this intricate synthesis procedure, the noteworthy participation of vitamin C with its sophisticated C=C double bond emerges as a pivotal reducing agent, while its resulting oxidized product (dehydroascorbic acid, DHAA) assumes the crucial roles of a stabilizer and captivates with its tethering ligand properties.[57]

3.5. Solvothermal Method

The hydrothermal method provides the foundation for solvothermal method. The key distinction is that the solvent of solvothermal method is organic solvent rather than water. A kind of high-pressure and high-temperature environment is created through the reaction still. In the solvothermal methodology, a multitude of factors exert considerable influence over the dimensions and structure of nanoparticles, encompassing elements such as reaction temperature, duration, and the inherent characteristics of the chosen solvent.

Tian et al. have developed a straightforward solvothermal technique for the production of exquisitely uniform ES-MIONs with a remarkable precision at the nanoscale, by utilizing iron acetylacetonate $Fe(acac)_3$ as the designated iron precursor, n-octanol as the solvent medium, and n-octylamine as the reductive agent.

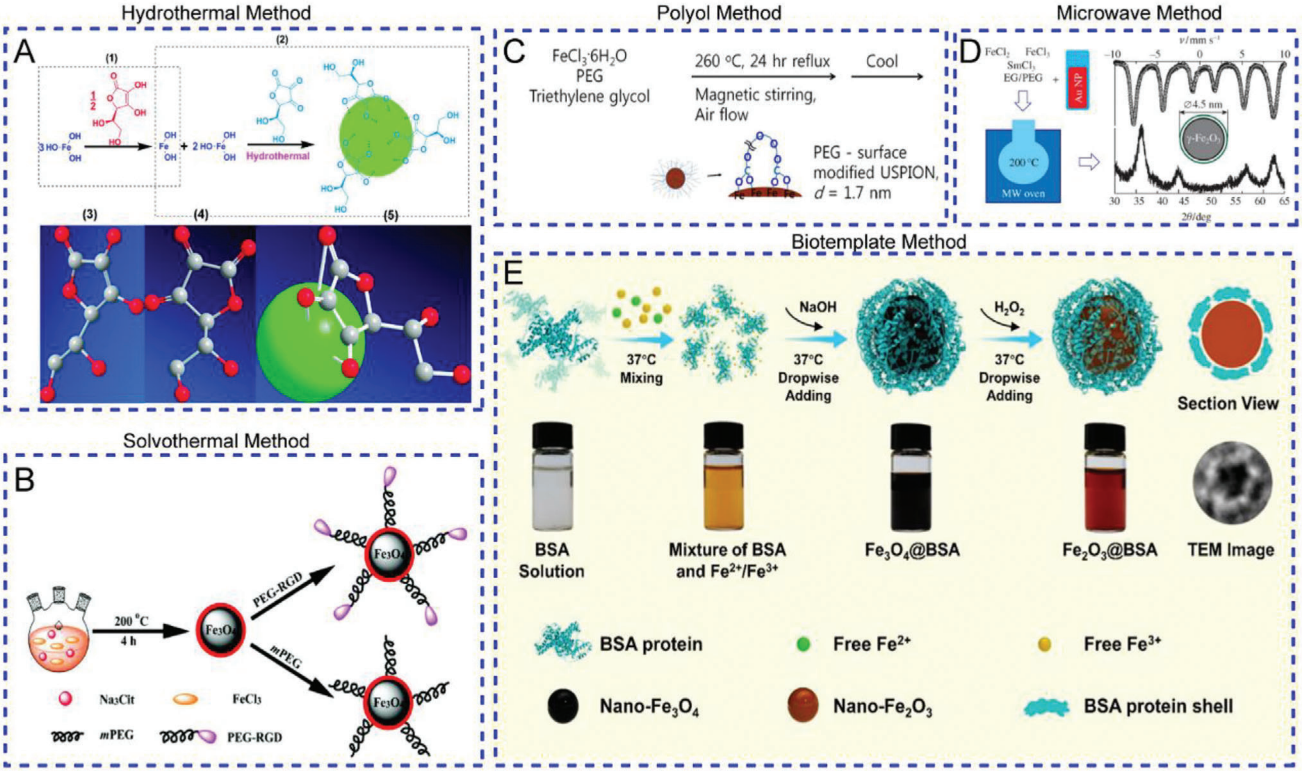

Figure 5. Extended synthesis mehods for ES-MIONs. A) Schematic representation of the preparation of ES-MIONs by vitamin C and DHAA. Reproduced with permission.[57] Copyright 2011, American Chemical Society. B) Schematic illustration of the preparation of Fe_3O_4-PEG-RGD and Fe_3O_4-mPEG. Reproduced with permission.[83] Copyright 2015, Royal Society of Chemistry. C) One-step synthesis of the PEG surface modified ES-MIONs. Reproduced with permission.[61] Copyright 2008, Institute of Physics Publishing. D) Microwave-assisted synthesis of Sm^{3+}-doped γ-Fe_2O_3 nanoparticles. Reproduced with permission.[63] Copyright 2018, Elsevier. E) Synthesized procedure of Fe_2O_3@BSA nanoparticles. Reproduced with permission.[68] Copyright 2020, American Chemical Society.

ES-MIONs with diameters of 4, 5, and 6 nm were produced in a sealed autoclave at 240 °C by changing the volume ratios of *n*-octylamine to *n*-octanol.[58]

Shi et al. successfully synthesized citrate-stabilized ES-MIONs with a size of 2.8 nm utilizing the solvothermal technique, while employing sodium citrate as an effective stabilizing agent. (Figure 5B). In the process, sodium citrate-stabilized ES-MIONs possess a negative potential of −39.7 mV and abundant —COOH groups on the ES-MIONs surface due to the citrate stabilization.

However, this process is conducted in a closed system that should prevent the volatilization of toxic gases and eliminate the sensitivity of reactants to oxygen. Due to the reaction being conducted in the reactor, the experimenter cannot directly observe the product during synthesis.

3.6. Microemulsion Method

Microemulsions are thermodynamically stable homogeneous mixtures consisting of a harmonious blend of oil, water, and surfactants. Microemulsions are formed by mixing the two immiscible solvents via surfactants without high shear conditions. The ES-MIONs are obtained in microemulsion bubbles after nucleation, agglomeration, and heat treatment.

J. Vidal-Vidal et al. developed a one-pot microemulsion method for producing oleylamine-coated ES-MIONs. A water-in-oil microemulsion (cyclohexane/Brij-97/aqueous phase) was selected for its stability with the aid of a non-ionic surfactant. The ES-MIONs are formed in the microreactors via the co-precipitation reaction with ferrous and ferric salts, and organic base oleylamine. The obtained ES-MIONs were coated with oleylamine showing a narrow size distribution (3.5 ± 0.6 nm), good crystal, and high M_s.[59]

Because the microemulsion bubbles can provide controlled “microreactors” that can limit nanoparticles’ growth and agglomeration, the synthesized products are usually spherical structures with uniform particle sizes. However, the major disadvantages of this method is the difficulty in scaling up nanoparticle manufacturing.

3.7. Polyol Method

The polyol method has emerged as an attractive synthesis method for ES-MIONs. The common polyols are ethylene glycol, diethylene glycol (DEG), triethylene glycol (TREG), and tetraethylene glycol (TEG).

Shen et al. developed an ultra-small, monodisperse, and water-dispersible ES-MIONs (size of 1.9 nm) in DEG solution. The prepared ES-MIONs display a good colloidal stability for a lengthy period of time in a variety of buffer solutions without undergoing any modifications.[60]

Park et al. innovatively engineered an exceptionally water-dispersible formulation of ES-MIONs by incorporating polyethylene glycol diacid (PEG) modifications. In their methodology, glycol was employed as a polar organic solvent, $FeCl_3 \cdot 6H_2O$ served as the iron precursor, and PEG was utilized as a hydrophilic surface coating (Figure 5C). By virtue of these modifications, the ES-MIONs exhibited remarkable monodispersity, with an average particle diameter of ≈1.7 nm.[61]

The utilization of polyols as solvents offers several advantages, including their capability to sustain high reaction temperatures and their ability to dissolve both organic and inorganic reagents. Moreover, polyols serve dual roles as both reductants and capping agents. Consequently, the ES-MIONs synthesized through this method typically possess a hydrophilic nature, rendering them highly suitable for various biomedical applications.[62]

3.8. Microwave Method

The microwave-assisted technique stands as a prompt, energy-efficient, and eco-friendly approach for the production of nanoparticles. In comparison to traditional furnace heating, microwave delivers quick and uniform heating to the solvents, allowing for homogenous nucleation and crystal formation in a significantly shorter time.

Lastovina et al. reported an ultra-small Sm^{3+}-doped ES-MIONs synthesis method by an MW-assisted one-pot polyol coprecipitation obtaining 4 nm of nanoparticles, as shown in Figure 5D.[63]

Bhavesh et al. proposed an incredibly fast microwave synthesis method for the preparation of ES-MIONs with a uniform size of ≈2.5 nm. The reaction was conducted by hydrazine-mediated reduction of the iron (III) chloride hexahydrate salt under microwave heating. The reaction is conducted at a temperature of 100 °C, utilizing a remarkably swift ramping time of a mere 54 s. This expeditious process eradicates any nonspecific reactions and augments the homogeneity of the sample. The ES-MIONs exhibit an elevated r_1 value of 5.97 $\text{mM}^{-1}\ \text{s}^{-1}$ and a diminished r_1 value of 27.95 $\text{mM}^{-1}\ \text{s}^{-1}$ at 1.5 Tesla, rendering them well-suited as a T_1 contrast agent in magnetic resonance imaging (MRI).[64]

Furthermore, Miao et al. developed a densely packed brush-like structure ES-MIONs via the microwave-assistant method. Due to the microwave, Fe^{2+} and Fe^{3+} ions are entirely coordinated with PAA. The final structure of ES-MIONs resembles a densely packed brush, with a varied inner structure of loops and tails. This high binding site prevents PAA dissociation from particles, even at high sterilization temperatures, and contributes to the microwave-assisted nanoparticles' stability. Benefiting from this "3D" structure, it provides significantly more space for free —COOH to absorb ferric ions, drastically reducing the iron ion discharge and ultimately enhancing security.[65]

3.9. Sol–Gel Method

The soluble iron salt precursor first suffers hydrolysis and polymerization reaction to form sol, then dehydration to form gel, and finally heated to obtain ES-MIONs in the sol–gel method. In the sol–gel process, auxiliary agents (e.g., surfactant citric acid) are often added to prevent the formation of large-size particles in the dehydration process. In addition, the sol system is needed to add acid or base to adjust the pH value. Despite the sol reaction being carried out at a low synthetic aging temperature, the gel also needs to be calcined at a high temperature to get the target product.

Tadic et al. reported highly crystalline and magnetic ES-MIONs with ≈4 nm size prepared via sol–gel method. First, the reaction system was a mixture of tetraethylorthosilicate (TEOS), water, ethanol, and iron nitrate ($Fe(NO_3)_3 \cdot 9H_2O$). After adjusting the pH of the mixture to 3, the transparent sol transformed into gel. Finally, The gel was heated to 900 °C to obtain the ES-MIONs. The ES-MIONs showed narrow size distribution with no nanoparticle agglomeration. The saturation magnetization M_s is 61.1 emu/g, which is convenient for targeted diagnostics and drug delivery.[66]

However, during the sol–gel synthesis process, the size and shape of ES-MIONs can be influenced by the pH value, reagents' concentration, and temperature. Though the sol–gel method is straight-forward, the sol–gel reaction is fast and difficult to regulate, resulting in non-uniform nanoparticles or an undesired gelation reaction.

3.10. Biotemplate Method

Biotemplate method is an intriguing process that uses proteins, bacteria, plants, or fungus to generate magnetite crystals. The Size and structure of ES-MIONs are depended on the used biotemplate.

For example, Yao et al. prepared ultrafine ferritin-based iron oxide (hematite/maghemite) nanoparticles using genetically recombinant human H chain ferritin. In the HFn protein cages, Fe^{2+} ions reacted with H_2O_2 at stoichiometric equivalents (H_2O_2:Fe^{2+} = 1:2). At a magnetic field strength of 7.0 T, the magnetoferritin that has been synthesized, boasting an averaged core size of ≈2.2 nm, displays an r_1 value of 0.86 $\text{mM}^{-1}\ \text{s}^{-1}$ and an r_2/r_1 ratio of 25.1.[67]

More conveniently, Xu et al. developed a kind of ES-MIONs (≈3.5 nm) using the bovine serum albumin (BSA) biotemplate in a more commercial way (Figure 5E). A nanocage structure can be formed by the BSA by using roughly 6–7 subunits of the BSA. In the nanocage, the ES-MIONs nanoparticles are prepared, which is similar to the synthesis process within ferritin cages. The size of ES-MIONs can be altered by adjusting the ratio of iron ions to BSA. What's more, the prepared ES-MIONs@BSA possess remarkable uniformity, exceptional monodispersity, excellent water solubility, and a pronounced T_1 contrast effect.[68]

Despite the environmentally friendly nature of this method, it is worth mentioning that the resultant particles may lack stability and uniformity, thereby exhibiting diminished homogeneity and heightened agglomeration.

4. Surface Modification of ES-MIONs

The coating of ES-MIONs is critical for ensuring biocompatibility and maintaining good performance during in vivo imaging. The

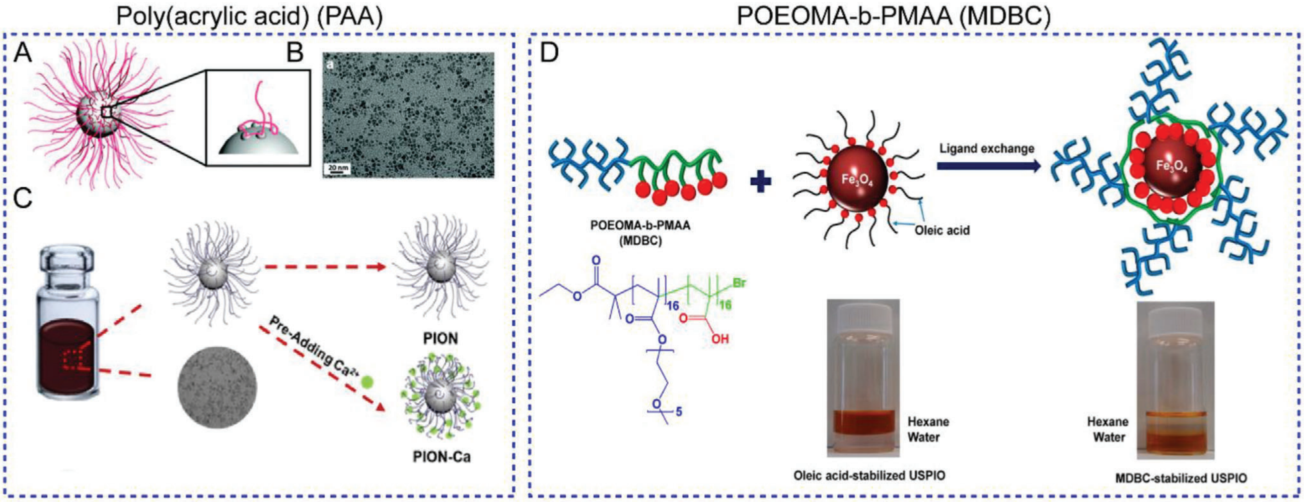

Figure 6. Schematic illustration of surface modification of ES-MIONs by artificial polymers. A) Conformation and TEM images (B) of PAA-coated ES-MIONs. Reproduced with permission.[65] Copyright 2019, Royal Society of Chemistry. C) The toxicity issue was resolved through pre-chelation of Ca^{2+} in PAA-coated ES-MIONs. Reproduced with permission.[74] Copyright 2019, Elsevier. D) The ES-MIONs stabilized with MDBCs via ligand exchange. Reproduced with permission.[75] Copyright 2014, American Chemical Society.

surface modification of the ES-MIONs is critical to maintaining the T_1-MRI performance. For the first aspect, the surface coordination molecules directly chelated on the ES-MIONs surfaces influence the water exchange rate ($k_{ex} = 1/\tau_M$) with the surroundings. For instance, the T_1 performance of ES-MIONs was significantly enhanced by a relatively high k_{ex} for the inner sphere.[69,70] For the second aspect, the ligand molecules chelated with ES-MIONs will prolong the rotational correlation time (τ_R), which will lead to a significantly enhanced r_1 value. For the third aspect, these ES-MIONs coated with different ligands can influence the stability, cellular uptake, tissue targeting, blood circulation, and metabolism ability in vivo.[71] For instance, the ES-MIONs that are coated with hydrophobic capping ligands display insolubility in water and pose a challenge to maintain stability in aqueous environments, primarily due to their strong tendency to agglomerate. Therefore, it was essential to develop a multi-functional ligand that confers biostability and enhanced T_1-MRI capability on ES-MIONs in the aqueous phase. Numerous sorts of molecules have been utilized for coating of ES-MIONs, including polymers (e.g., polyethylene glycol, poly(acrylic acid), polysaccharides, zwitterion polymers), and functional proteins.

4.1. Artificial Polymers

Polymer grafting is widely regarded as one of the most effective methods for ES-MIONs surface functionalization. Among multitudinous kinds of polymers, polyethylene glycol (PEG), polyacrylic acid (PAA), and multidentate block copolymers (MDBCs) were most widely used for the modification of ES-MIONs.

4.1.1. PEG

Lydia Sandiford et al. successfully achieved surface PEGylation of ES-MIONs using 1,1-bisphosphonates (BPs) with a strong attraction for oxide ions. These ES-MIONs remain stable in water or saltwater for a minimum of seven months post-PEGylation and exhibit a close-to-zero ζ-potential at neutral pH. The measured r_1 and r_2/r_1 values are 9.5 mM^{-1} s^{-1} and 2.97, respectively, indicating the promising potential of PEG-coated ES-MIONs as T_1 -weighted MRI contrast agents.[72]

Taeghwan Hyeon et al. also reported the PEGylated ES-MIONs with a diameter of ≈3 nm, showed a stable state in aqueous media and increased blood half-live in blood. The ES-MIONs are mostly localized in the spleen, and caused solely stress-related effects, with no further serious consequences. Accompanied by their PEGylation, the ES-MIONs manifest a remarkable capacity to serve as a T_1 contrast agent, presenting a promising avenue for future clinical diagnostics.[73]

4.1.2. Poly(Acrylic Acid)

Gu et al. developed a poly(acrylic acid) (PAA)-coated ES-MIONs (size ≈4.5 nm) for T_1-weighted MRI with well stability in physiological conditions (**Figure 6**A,B).[65] However, PAA is a polyelectrolyte and displays a counter-ion confinement effect because of its abundant carboxyl groups. By absorbing ions in a large quantity of solution, PAA macromolecule has the potential to disrupt the electrolyte balance in our bodies Following a sequence of experiments, it was shown that PAA-coated ES-MIONs exhibited cardiac toxicity upon intravenous injection Gu et al. further proposed an appropriate solution for preparing pre-chelation Ca^{2+} ($n_{(Ca)}$: $n_{(COOH)}$ = 3: 8) to ES-MIONs to solve this deadly effect (Figure 6C). The Ca^{2+} chelated ES-MIONs demonstrates significantly enhanced cardiac and electrophysiological safety, broadening the application of -COOH decorated nanoparticles in vivo.[74]

4.1.3. Multifunctional Block Copolymers

Chan et al. have developed novel ES-MIONs that are stabilized using multidentate block copolymers (MDBCs). Within

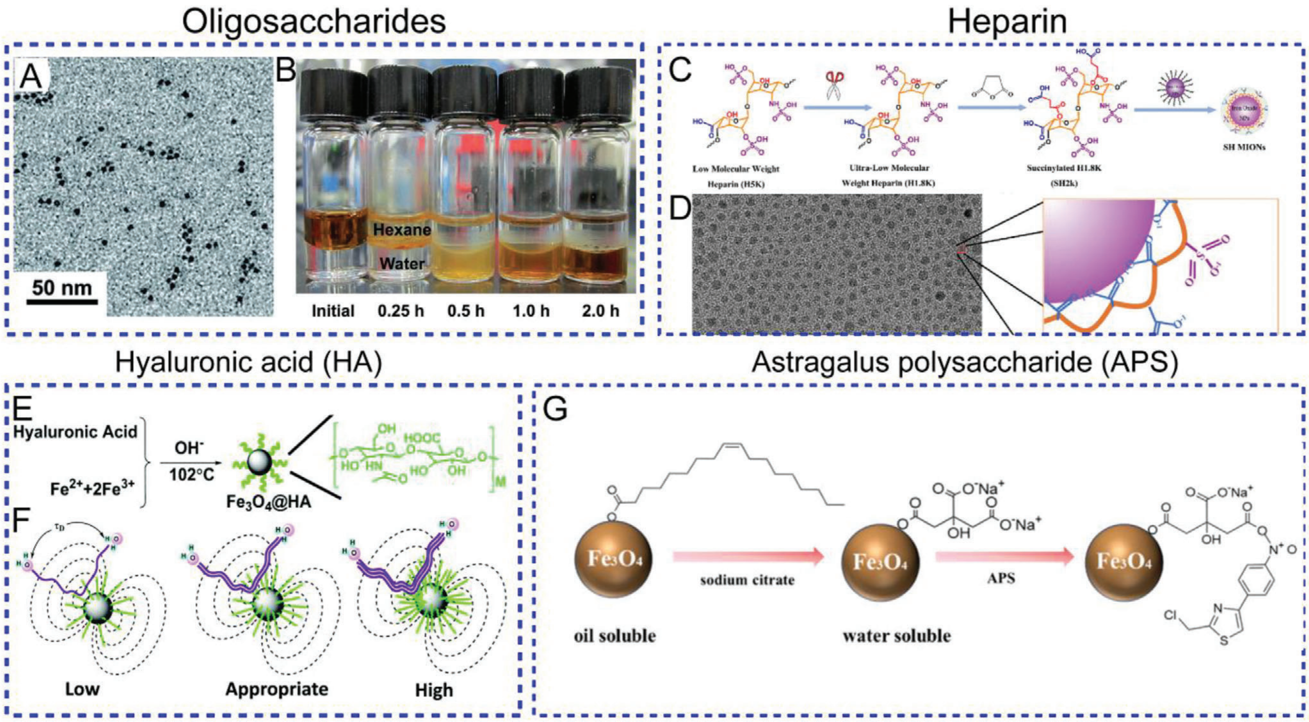

Figure 7. Schematic illustration of surface modification of ES-MIONs by natural polymers. A) The TEM images of oligosaccharides-coated ES-MIONs and B) solvent phase transition from organic phase hexane to the aqueous solution. Reproduced with permission.[76] Copyright 2014, Royal Society of Chemistry. C) Preparation of ultralow-molecular-weight heparin monolayer-coated ES-MIONs. D) TEM image and zoomed view of the surface binding mode for heparin-coated ES-MIONs. Reproduced with permission.[78] Copyright 2020, American Chemical Society. E) Preparation of hyaluronic acid-coated ES-MIONs and F) illustration of the translational diffusion time influenced by the density of surface ligand. Reproduced with permission.[79] Copyright 2017, Royal Society of Chemistry. G) Schematic illustration of design of APS-coated ES-MIONs. Reproduced with permission.[80] Copyright 2019, American Chemical Society.

these MDBCs, there is a combination of an anchoring block and a hydrophilic block. The anchoring block is comprised of pendant carboxylates as multidentate anchoring moieties, capable of forming robust bonds with the surfaces of ES-MIONs. (Figure 6D). In contrast, the hydrophilic block is composed of pendant hydrophilic oligo(ethylene oxide) chains, which confer water dispersibility and augment biocompatibility. ES-MIONs coated with MDBCs demonstrate exceptional long-term colloidal stability under biologically conditions (diverse electrolyte concentration, pH, and temperature).[75]

4.2. Natural Polymer

4.2.1. Oligosaccharides

Huang et al. fabricated ES-MIONs (≈3.5 nm in size) coated with oligosaccharides via in situ polymerization of glucose on the surface of ES-MIONs (**Figure** 7A). By employing the “in situ polymerization” coating method, glucose can directly generate oligosaccharides on the hydrophobic iron oxide nanoparticles surface, leading to remarkable water solubility, biocompatibility, and exceptional stability of the ES-MIONs (Figure 7B). These oligosaccharide-coated ES-MIONs exhibit an r_1 value of 4.1 mM^{-1} s^{-1} and a low r_2/r_1 ratio of 4.0 at 3.0 T. Importantly, these ES-MIONs are cleared in the body quicker than those with greater diameter, implying improved safety for clinical applications.[76]

4.2.2. Heparin

Heparin is a linear polysaccharide that has long been utilized as an anti-coagulant in clinical. Heparin has been widely employed in nanoparticles’ surface modification for its colloidal stability, well bio-acceptability, easy chemical modification, and high negative charge. Hugo et al. prepared ES-MIONs coated with various lengths of heparin (HEP) by depolymerization reaction for T_1-weighted MRI. Interestingly, ES-MIONs coated with the intermediate length of HEP (degree of polymerization is 19, Mn ≈5.5 kDa) exhibit a well-balanced profile, demonstrating minimal uptake by non-specific organs and efficient urinary clearance. Due to its extended blood half-life, the heparin-coated ES-MIONs achieved a moderate level of accumulation in the tumor, effectively striking a balance between T_1-MRI contrast ability and pharmacokinetic properties.[77]

Dai et al. present ultralow-molecular succinylated HEP-coated ES-MIONs (Figure 7C), which exhibit a high r_1 of 4.6 mM^{-1} s^{-1} and a low r_2/r_1 ratio of 4.0 at 7.0 T. The hydrophilic succinylated HEP potentiated interactions with the water core by facilitating unhindered water flow towards the iron surface (Figure 7D), thereby amplifying the T_1-MRI effect. In addition, the

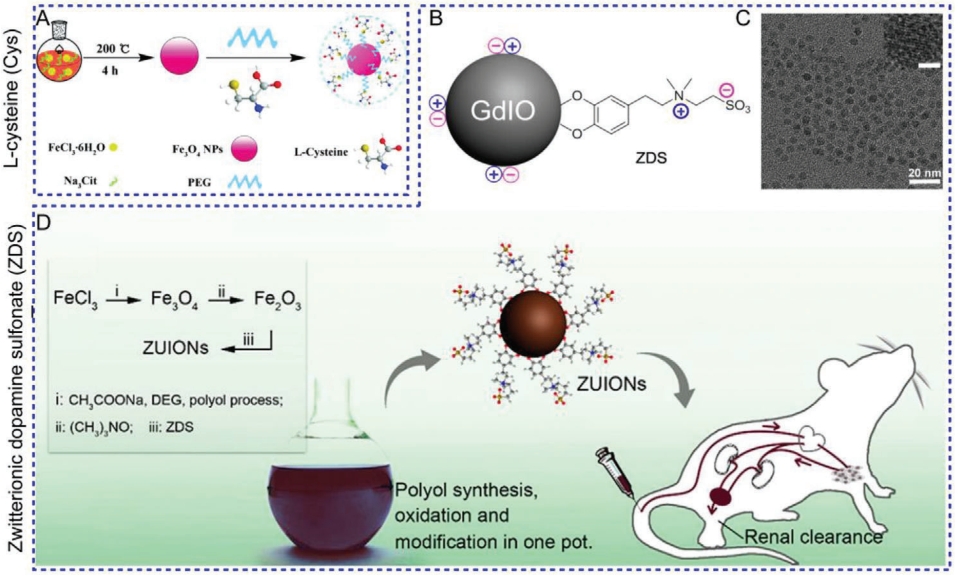

Figure 8. A) Schematic illustration of the preparation of the zwitterions-coated ES-MIONs. Reproduced with permission.[44] Copyright 2017, Royal Society of Chemistry. B) Schematic illustration of spin phenomena in small-sized GdIO nanoparticles and structure of GdIO nanoparticles coated with zwitterionic dopamine sulfonate (ZDS) molecules. C) TEM images of 4.8 nm GdIO nanoparticles. Reproduced with permission.[81] Copyright 2013, American Chemical Society. D) Schematic illustration of the one-pot synthesis of ZES-coated ES-MIONs and their application as T_1-MRI CAs. Reproduced with permission.[82] Copyright 2018, American Chemical Society.

succinylated ultralow-molecular HEP-coated ES-MIONs (core ≈2 nm) showed significantly meliorative T_1-weighted MRI sensitivity of tumor and bladder over 90 min. What's more, the excretion of the ES-MIONs appeared to begin, and the ≈65% dose was eliminated over 2 days.[78]

4.2.3. Hyaluronic Acid

Zhou et al. synthesized four kinds of hyaluronic acid (HA) coated ES-MIONs with different HA densities via co-precipitation method (Figure 7E). Surprisingly, they discovered that the surface density of HA on ES-MIONs was an important element in adjusting T_1- and T_2-weighted MRI performance by influencing the water translational diffusion time (τ_D). As depicted in Figure 7F, when the surface ligand density is low (indicated by a single line), the diffusion of water molecules becomes straightforward. However, this situation becomes more intricate when the surface ligand density is high (represented by three lines). Conversely, when the surface ligand density is optimal for nanoparticle separation (represented by two lines), the translational diffusion rate becomes conducive for augmented T_1-MRI effects.[79]

4.2.4. Astragalus Polysaccharide

Jiang et al. developed an astragalus polysaccharide (APS) coated ES-MIONs (Figure 7G), showing the efficiency of the therapeutic drug for iron deficiency anemia (IDA) treatment. The T_1 and T_2-MRI images showed dual enhancement in the stomach and the bowels for the gastric infusion mouse, compared to the normal mouse. Furthermore, the APS-coated ES-MIONs demonstrate a pronounced therapeutic efficacy in IDA treatment, owing to the combined benefits derived from iron element supplementation mediated by Fe_3O_4 and the APS-induced generation of hematopoietic cells.[80]

4.3. Zwitterions

Zwitterionic molecules, which possess an equal number of negative and positive groups, exhibit a multitude of water molecules that are encompassed through hydrogen bonding. Therefore, zwitterions have the ability to establish a densely-structured aqueous protective shell encircling the ES-MION, thus endowing ES-MIONs with notably decreased adsorption and exceptional antifouling properties.

4.3.1. Cysteine

Ma et al. developed a facile method to produce Cysteine (Cys)coated ES-MIONs (size ≈3.2 nm) for angiography and tumor MRI (**Figure 8**A). The ES-MIONs were sequentially functionalized with NH_2-PEG-Mal (PEG-modified with an amine group at one end and a maleimide group at the other end) and Cys. Compared to ES-MIONs-mPEG, the Cys-coated ES-MIONs (with a core size of ≈3.2 nm) exhibit a favorable r_1 value of 1.2 mM^{-1} s^{-1}, along with exceptional stability, biocompatibility, antifouling properties.[44]

4.3.2. ZES

Wei et al. developed zwitterion (ZES) coated ES-MIONs (ZES-ES-MIONs) as T_1 contrast agent, which comprised inorganic cores

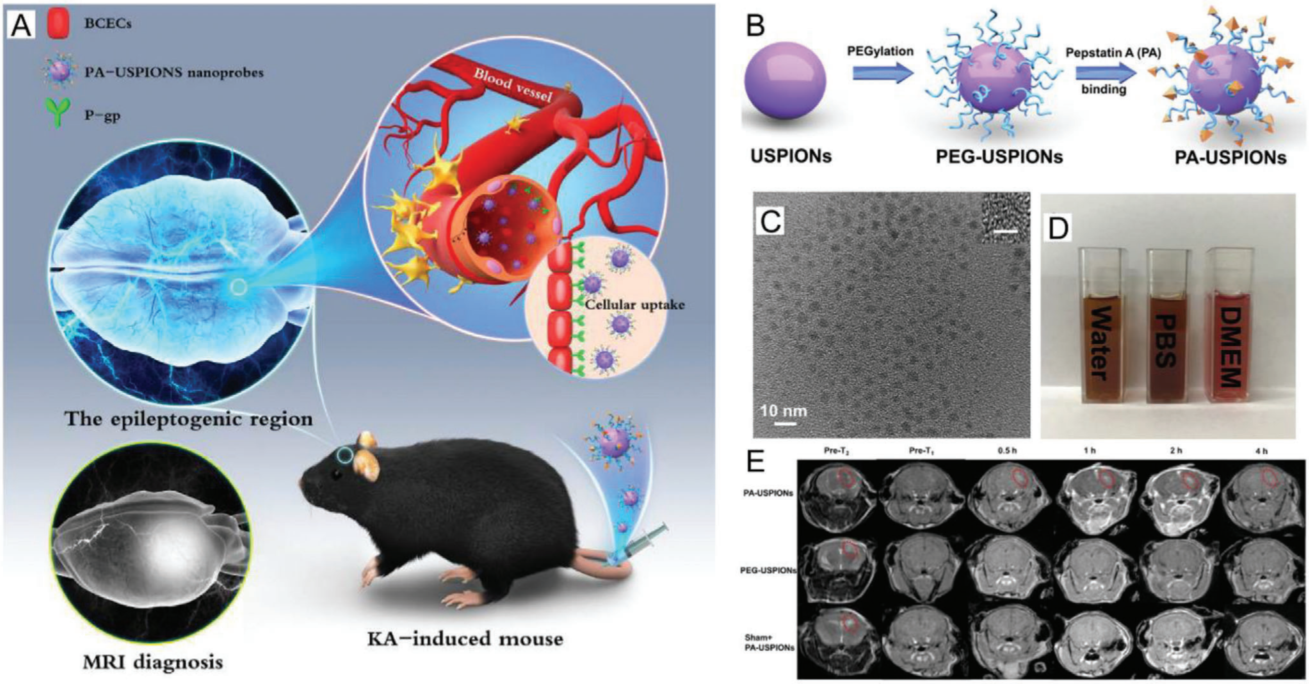

Figure 9. A) Schematic diagram of the PA-coated ES-MIONs for T_1-weighted positive MR imaging in epileptogenic region. B) The fabrication process, C) TEM images, and D) dispersibility of PA-coated ES-MIONs. E) T_1- and T_2-weighted MR imaging of the epileptogenic region for PEG-coated ES-MIONs and PA-coated ES-MIONs. Reproduced with permission.[42] Copyright 2020, Elsevier.

inorganic cores of ≈3 nm in size and ultrathin hydrophilic shells of ≈1 nm. The results of biodistribution experiments using ^{59}Fe radioisotope-labeled ZES-ES-MIONs suggest that the majority of ZES-ES-MIONs are cleared through the renal route, avoiding long-term contrast changes. In addition, the iron dose remaining in the body can be kept in a safe range.[56]

Gao et al. developed zwitterion-coated nanoparticles called gadolinium-embedded iron oxide (GdIO) nanoparticles (Figure 8B). These nanoparticles possess a small size and demonstrate a robust T_1-MR imaging ability. Following the application of zwitterionic dopamine sulfonate molecules as a coating, the GdIO nanoparticles exhibited a consistent hydrodynamic diameter of ≈5.2 nm in both PBS and fetal bovine serum (Figure 8C). This observation suggests minimal nonspecific protein absorption, indicating the nanoparticles' low propensity for binding to proteins. The GdIO nanoparticles coated with zwitterions demonstrated relatively lengthy circulation half-lives of ≈50 min. In addition, they exhibited efficient passive targeting toward tumors and also exhibited the potential for rapid renal clearance following tumor imaging.[81]

Hao et al. introduced a one-pot gram-scale synthesis method for producing zwitterion-capped ES-MIONs, as illustrated in Figure 8D. These ES-MIONs possess a remarkably small core size of 3.7 nm and demonstrate excellent colloidal stability across a range of buffers. The ES-MIONs exhibit a desirable r_1 value of 2.4 mM^{-1} s^{-1} and an impressive r_2/r_1 ratio of 2.2 at 1.0 T, ensuring their suitability as T_1 magnetic resonance imaging contrast agents. The zwitterion-capped ES-MIONs also exhibited substantial contrast enhancement in the blood pool and were then primarily eliminated from the body via the renal excretion system. The ES-MIONs have several advantages, such as exceptional biocompatibility, a robust T_1-MRI contrast effect, suitable circulation time, and the ability to be cleared through the renal pathway.[82]

4.4. Functional Peptide

Shi et al. reported RGD-functionalized ES-MIONs for targeted T_1-weighted MR imaging of gliomas characterized by an overexpression of $\alpha_v\beta_3$ integrin. In the synthesis procedure, the stable sodium citrate-stabilized ES-MIONs were conjugated with PEGylated RGD. The RGD-functionalized ES-MIONs with a size of ≈2.7 nm, exhibited favorable characteristics such as excellent water dispersibility, colloidal stability properties, cytocompatibility, and hemocompatibility, which served as a targeted nanoprobe for $\alpha_v\beta_3$ integrin-overexpressing gliomas.[83]

In addition, Chen et al. prepared a specific peptide (i.e., EGFR peptide) coated ES-MIONs (≈3.5 nm) for targeted T_1-weighted MRI of hepatocellular carcinoma (HCC). The EGFR peptide is attached to the PEG chain via a thioether-maleimide reaction. In the HCC xenograft tumors, ES-MIONs showed a tumor uptake peak at ≈2 h and a rapid elimination at ≈24 h.[84]

Furthermore, Du et al. successfully conjugated Pepstatin A (PA) onto the surface of PEGylated ES-MIONs to construct a T_1-MRI nanoprobe (**Figure 9**A). PA is a compact peptide known for its specific binding affinity to P-glycoprotein (P-gp), which is overexpressed in the epileptogenic region. The as-prepared ES-MIONs possess an average size of ≈3.63 nm and high stability in DMEM medium even for over 30 days (Figure 9B–D). The PA-coated ES-MIONs have an enhanced T_1-MRI contrast with high r_1 compared with the commercial Gd-DTPA contrast agent (Figure 9E).[42] Following the injection of PA-coated ES-MIONs in vivo, the signal-to-noise ratio of the epileptogenic region exhibited a rapid and significant increase. The maximum enhancement, approximately twofold stronger than the group injected with non-targeted PEG-USPIONs, was observed at ≈2 h (Figure 9F).

5. Enhancement Strategies for ES-MIONs-Based T_1-MRI

Besides the above-mentioned surface chemistry to enhance T_1-MRI ability of ES-MIONs, some intelligent strategies were also applied to obtain a better T_1-MRI capability based on ES-MIONs, such as structural remodeling (e.g., nanoclusters, nanowires, or dotted core-shell nanoparticles), metal ion doped nanoparticles, T_1/T_2 dual-mode MRI, and contrary contrast-MRI (CC-MRI).

5.1. T_1-MRI Enhanced by Structural Remodeling

5.1.1. Nanoclusters

Although the ES-MIONs nanoparticles exhibit strong T_1 enhancement, their performance as T_1 contrast agents is affected by several issues. First, ES-MIONs can be quickly metabolized through the kidney, limiting their application in prolonged in vivo tracking. Swift elimination through renal clearance has been a persistent challenge encountered by numerous nanoparticles of diminutive proportions. Furthermore, the proclivity of ES-MIONs nanoparticles to aggregate poses a noteworthy apprehension, owing to their elevated surface energy. In the event of aggregation, the T1 capabilities of ES-MIONs shall be compromised. The nanocluster systems addressed the fast renal clearance issue, and minimized the direct aggregation issue. The nanoclusters can be made in a spherical and layered shape.

J. Sherwood et al. presented a spherical nanocluster by crosslinking monodispersed tannic acid-coated ES-MIONs (<4 nm) with bovine serum albumin (BSA; **Figure 10**A), forming nanoclusters (≈200 nm). The T_1 performance of ES-MIONs was enhanced by the hydrophilic tannic acid and BSA, which facilitated water exchange. Moreover, through the cross-linking of ES-MIONs nanoclusters with BSA, the T_1 functionality was preserved while concurrently prolonging the duration of bloodstream circulation from a mere 15 minutes to an impressive span exceeding 2 h.[85]

Similarly, Zhang et al. developed a novel layered nanoplatform, in which ES-MIONs were stabilized on layered double hydroxide (LDH) nanosheets (Figure 10B). The r_1 value of LDH- Fe_3O_4 is 5.53 $\text{mM}^{-1}\ \text{s}^{-1}$, significantly surpassing that of Fe_3O_4 (0.42 $\text{mM}^{-1}\ \text{s}^{-1}$). This substantial increase in r_1 can be attributed to the presence of LDH, which enhances the spacing between Fe_3O_4 nanoparticles and reduces magnetic coupling. Consequently, LDH promotes a smaller effective magnetic size compared to pure Fe_3O_4 nanoparticles. In addition, this LDH nanosheet exhibits prolonged accumulation at the tumor site, offering potential advantages for subsequent chemotherapy treatments.[86]

Recently, Chen et al. presented a lamellar-shaped nanocluster system that combines engineered graphene oxide with in situ growth of ES-MIONs. for T_1-MRI and pH-sensitive tumors treatment (Figure 10C). The GO nanosheets decreased the M_s of ES-MIONs due to the spin canting effect. The interface effect, energy exchange (e.g., thermal exchange), and the charge transfers between ES-MIONs and GO also increased the r_1 value. The tumor T_1-MRI presented noticeable enhancement in tumor even at 90 min, which is longer than the commercial gadoteric acid (Gd-DOTA), which typically lasts approximately 40 minutes.[87]

To prevent the rapid elimination of pure ES-MIONs from the body through renal clearance. Zhou et al. developed an exosomes (Exo) encapsulated ES-MIONs nanoclusters (Exo@ESIONs). The blood circulation half-lives of Exo@ESIONs and ES-MIONs are found to be 6.8 and 1.4 h, respectively. In the Exo@ESIONs group, the T_1 signal in the tumor progressively increased over time and peaked at 4 hours after injection, demonstrating superiority over pure ES-MIONs. This is because the pure ES-MIONs are rapidly cleared through the renal-urinary system.[88]

5.1.2. Nanowires

Hu et al. synthesized a biodegradable Fe-doped MoO_x (FMO, ≈450 nm of length) ultrafine nanowires for cancer therapy using a one-step solvothermal method (Figure 10D). After injection of FMO, the tumor site exhibited a robust positive T_1-MRI signal. In addition, The FMO material had an outstanding photothermal conversion efficiency and chemodynamic therapy (CDT) ability in tumors.[89]

5.1.3. Dotted Core–Shell Nanoparticles

Dotted core–shell nanoparticles based on ES-MIONs were also developed to enhance the T_1 MRI capability. Shen et al. developed a core–shell nanoparticle with a dotted structure, where the core consisted of ES-MIONs and the shell was composed of Gd oxide nanoparticles. The Gd oxide nanoparticles were synthesized in situ on the surfaces of ES-MION seeds. An RGD dimer (RGD2) was conjugated on the surface of the dotted core–shell nanoparticles to realize tumor-active targeting (Figure 10E). The r_1 value of the FeGd-HN3-RGD2 nanoparticles is 70.0 $\text{mM}^{-1}\ \text{s}^{-1}$, significantly surpassing the r_1 values of both commercially available and previously reported T_1-weighted MRI contrast agents.[90]

Zou et al. employed an inverse mini-emulsion technique and Michael addition reaction to fabricate hybrid nanogels (NGs) incorporating ES-MIONs, utilizing polyethylenimine (PEI) as the base material. The PEI NGs were covalently conjugated onto the ES-MIONs surface via acetylation reaction. The obtained dotted core–shell nanoparticles showed higher r_1 value and improved MRI imaging sensitivity compared with free ES-MIONs, which could be due to the increased molecular volume of ES-MIONs, leading to prolonged τ_R.[91]

5.2. T_1-MRI Enhanced by Metal Ion-Doped Nanoparticles

To enhance the T_1-MRI capability of ES-MIONs, the composition of ES-MIONs can be optimized. Miao et al. reported chemically

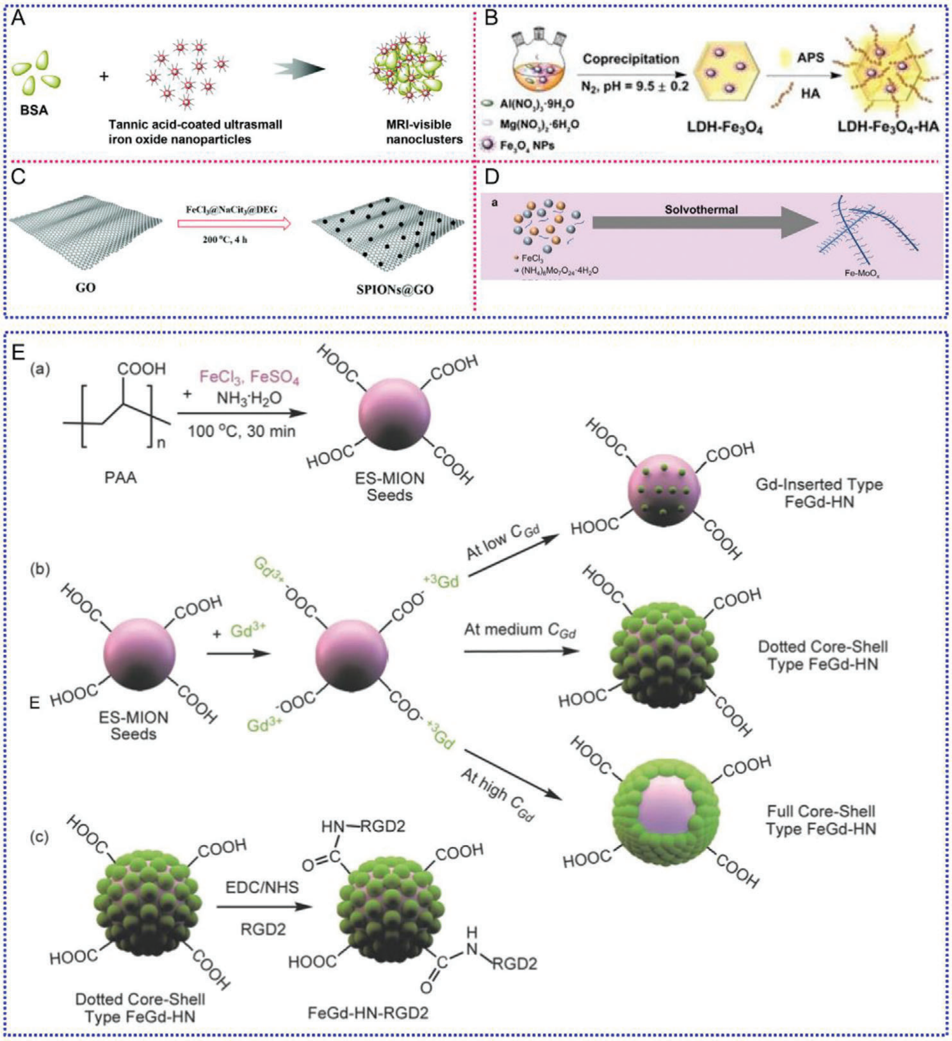

Figure 10. A) Illustration of BSA-crosslinked nanocluster formation process. Reproduced with permission.[85] Copyright 2017, Royal Society of Chemistry. B) Synthetic procedure and theranostic mechanism of LDH-Fe_3O_4-HA/DOX nanoplatforms. Reproduced with permission.[86] Copyright 2020, Ivyspring International Publisher. C) Schematic illustrations of the preparation of CAD-SPIONs@GO for breast tumor diagnosis and therapy. Reproduced (Adapted) with permission.[87] Copyright 2019, Royal Society of Chemistry. D) Synthesis process of FMO nanowires and schematic illustration FMO for photothermal enhanced CDT and GSH-depleted amplified CDT. Reproduced with permission.[89] Copyright 2021, Wiley-VCH. E) Schematic illustration of synthesis steps of our RGD2-conjugated dotted core–shell type ES-MION/GdON hybrid nanoparticles. Reproduced with permission.[90] Copyright 2018, Wiley-VCH.

engineered ES-MIONs (≈3.8 nm) with a controlled dopant composition in the crystalline core and a disordered shell, aiming to enhance the T_1 effect. (**Figure 11**A–D). Both the increased magnetization value caused by Zn^{2+} doping and reduced τ_m caused by Mn^{2+} substitution could effectively modulate the r_1 relaxivity of ES-MIONs (Figure 11E,F). Significantly, the optimized ES-MIONs, featuring a Zn-doped core and Mn-substituted shell, exhibited an impressive r_1 value of 20.22 mM^{-1} s^{-1}, surpassing that of clinically used gadolinium-based T_1 contrast agents.[92]

Fan et al. developed a nanoprobe for T_1-weighted MRI that exhibits enhanced signal amplification functions at multiple levels, enabling the visualization of ultrasmall breast cancer metastases. (Figure 11G). The ES-MIONs nanoprobe (≈3.9 nm) was synthesized based on the dynamic simultaneous thermal decomposition (DSTD) method with doping of Fe^{3+} and Mn^{2+}. The ES-MIONs nanoprobe exhibits a significantly higher r_1 value of 6.79 mM^{-1} s^{-1} compared to γ-Fe_2O_3-CREKA (3.79 mM^{-1} s^{-1}) due to manganese doping, indicating its potential as a high-performance T_1-weighted MRI nanoprobe. Furthermore, within the distinctive pathological environment of metastases, the Mn^{2+}-doped ES-MIONs demonstrate the capability to release Mn^{2+} ions. Upon binding with proteins within cancerous tissues, the accumulated Mn^{2+} ions exhibit the capability to enhance the brightness of metastatic sites.[93]

5.3. T_1/T_2 Dual-Mode MRI

ES-MIONs show strong T_1 contrast effect, but very low T_2 contrast due to the small superparamagnetism. Although the

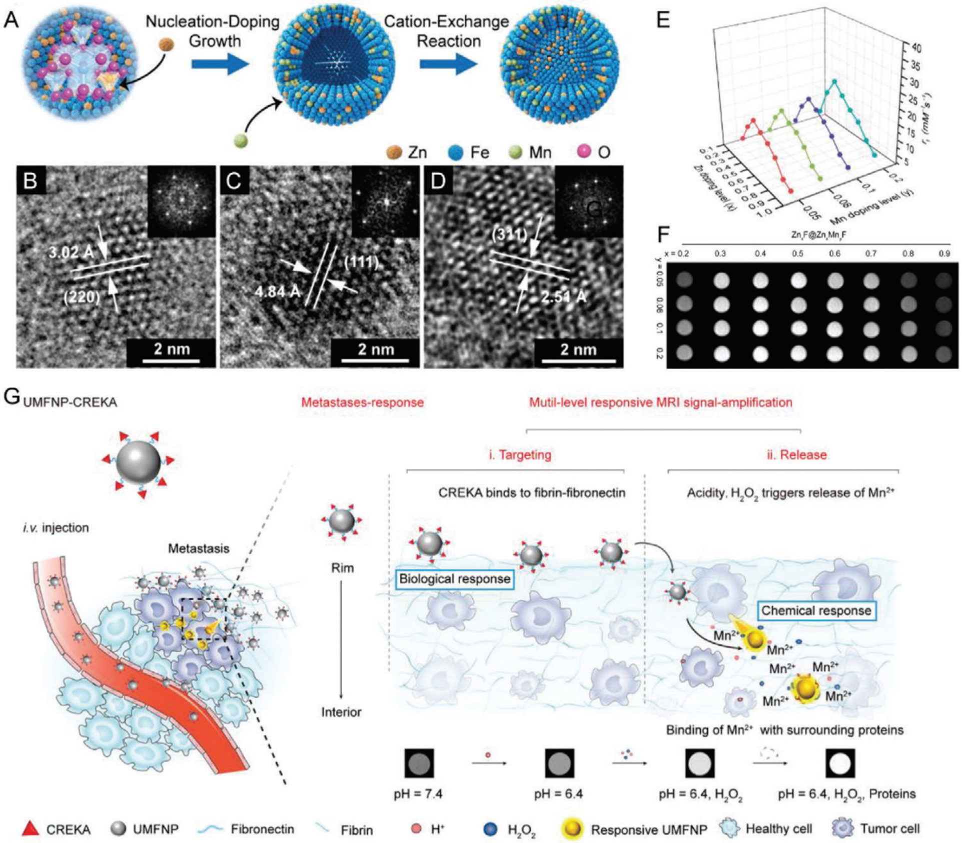

Figure 11. A) Schematic illustration of the chemically engineered ES-MIONs with the dopant-controlled crystalline core and disordered shell with the dopped Zn and Mn elements. High-resolution TEM images of Zn$_{0.4}$F (B), γ-Fe$_2$O$_3$@Mn$_{0.4}$F (C), and Zn$_{0.4}$F@Zn$_{0.4}$Mn$_{0.2}$ F (D). MR contrast enhancement effects of Zn$_x$F@ZnxMn$_y$F. E) Plot of r_1 value as a function of Zn doping level (x) and Mn-substituted level (y) of Zn$_x$F@Zn$_x$Mn$_y$F. F) T_1-weighted images of Zn$_x$F@Zn$_x$Mn$_y$F (C$_{[\text{Zn+Mn+Fe}]}$ = 0.5 mм). Reproduced with permission.[92] Copyright 2021, American Chemical Society. G) Schematic illustration of the Mn-dopped ES-MIONs with multilevel responsive T_1-weighted MR signal-amplification capabilities for illuminating ultrasmall metastases. Reproduced with permission.[93] Copyright 2020, Wiley-VCH.

T_2 contrast agent provides the dark contrast that is useless to lighten tumor tissue, it still provides a referential information to distinguish tissue structure in some complicated condition.[94] Moreover, in contrast to other multimodal imaging technologies such as MR/optical and MR/PET, T_1-T_2 dual-mode MRI offers the advantage of simultaneous imaging using a single instrument system. This approach helps eliminate variations in penetration depths and spatial/time resolutions that arise from utilizing multiple imaging devices.[95] Therefore, in comparison to single-mode contrast agents, T_1-T_2 dual-mode MRI contrast agents have the potential to greatly enhance diagnostic accuracy. This is achieved by offering anatomical images at equivalent levels, but with distinct contrasts, thereby providing self-validated information. Nevertheless, the development of T_1-T_2 dual-mode contrast agents has posed significant challenges. First, the combination of T_1 and T_2 contrast agents presents a challenge due to the strong magnetic coupling between them. This coupling can disrupt the relaxation effect of the paramagnetic T_1 contrast agent, leading to undesired suppression of the magnetic resonance signal.[96] Second, it is essential to ensure optimal relaxation parameters, wherein both r_1 and r_2 values should be maximized, and the r_2/r_1 ratio should ideally fall within the range of 5–10.[97] Fortunately, ES-MIONs could inherently display T_1- and T_2- weighted imaging abilities with appropriate sizes and M_s. Shi et al. realized the T_1/T_2-weighted MRI by enhancing the retention of ES-MIONs in pathological tissue (**Figure 12**A). First, citric acid-stabilized ES-MIONs were produced and modified with folic acid (FA) and diazirine (DA) through a coupling reaction. After intravenous delivery, the monodispersed ES-MIONs traversed the vasculature and effectively infiltrated the inflamed area associated with arthritis, showing T_1-weighted MRI imaging. Upon exposure to 405 nm laser irradiation, the ES-MIONs assembled in the inflammation region, offering a dual-mode T_1/T_2-weighted precision MRI.[98]

Generally, the T_1-MRI sensitivity of ES-MIONs is diminished under an ultrahigh magnetic field (UHF,≥7.0 T). Consequently, Wang et al. developed specialized contrast agents (CAs) that exhibit robust T_1 contrast and moderate T_2 contrast, specifically designed for ultra-high field (UHF) MRI. (Figure 12B). The nearly paramagnetic core of ES-MIONs guarantees low magnetization, resulting in moderate T_2 relaxation of the adjacent water protons. In addition, ES-MIONs surface was modified with citric acid and PEG to extend water molecule lifetime in the second sphere (τ'_m), which accelerates T_1 relaxation of water protons. This

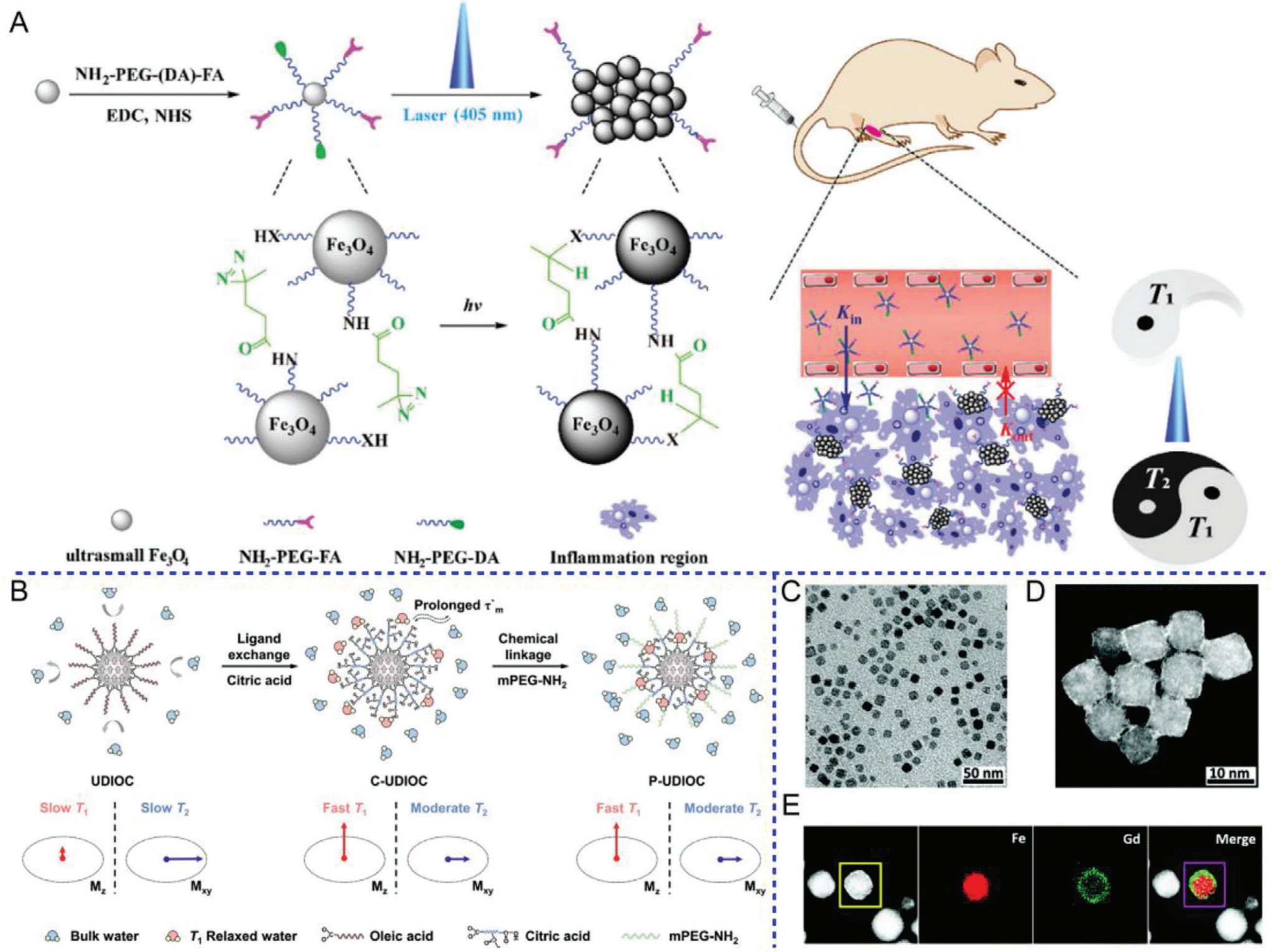

Figure 12. A) Schematic illustration of the synthesis of Fe_3O_4-PEG-(DA)-FA NPs for enhanced retention and tunable T_1/T_2-weighted MR imaging. Reproduced with permission.[98] Copyright 2019, Wiley-VCH. B) Schematic illustration of the fabrication process of hydrophobic surfactants of UDIOC and hydrophilic P-UDIOC. The P-UDIOC facilitates fast T_1 and moderate T_2 relaxation of water protons, leading to high-performance T_1/T_2 dual-contrast effect under UHF. Reproduced with permission.[99] Copyright 2021, Wiley-VCH. C) Representative TEM image, D) STEM-HAADF image, and E) EDX mapping images of Fe_3O_4/Gd_2O_3 core/shell nanocubes. Reproduced with permission.[100] Copyright 2016, Royal Society of Chemistry.

modification enables a dual enhancement of T_1 and T_2 contrast effects at ultra-high field (UHF). On the one hand, the interaction of the uncoordinated carboxylic group of citric acid with water protons through hydrogen bonds would enhance τ'_m, resulting in an accelerated T_1 relaxation of water protons. Conversely, the magnetization of ES-MIONs has a sharp increase with the external magnetic field, leading to an exceedingly strong T_2 contrast effect under UHF.[99]

Liang et al. developed a novel synthesis method for core/shell Fe_3O_4/Gd_2O_3 nanocubes, enabling dual-modal T_1/T_2 MRI imaging. (Figure 12C–E). The Fe_3O_4 content is mainly aggregated in the core served as T_2-MRI agents, while Gd_2O_3 is dispersed on the nanocube surface served as T_1-MRI agents. The cubic nanoparticle displays a synergistic augmentation of its T_1/T_2 dual-mode contrast effect, owing to its substantial surface-to-volume ratio and efficacious radius.[100]

5.4. Contrary Contrast-MRI (CC-MRI) Strategy

Although there are certain advantages to using T_1/T_2 dual-mode MRI contrast agents (CAs) with high r_1 and r_2 values, they still face certain problems: 1) Performing T_1/T_2 dual-mode MRI requires executing T_1-weighted and T_2-weighted sequences with distinct scanning parameters, resulting in increased workload for busy clinical MRI machines. 2) Physicians often face greater technical challenges in diagnosing using both T_1 and T_2 images compared to single-mode images. 3) the T_1 and T_2 signals from T_1/T_2 dual-mode contrast agents typically exhibit mutual suppression due to the positive and negative nature of their respective signals. In order to solve the above-mentioned problems of T_1/T_2 dual-mode MRI, Shen et al. introduced a novel concept known as the contrary contrast-MRI (CC-MRI) strategy, wherein CC-MRI contrast agents exhibit a positive or negative signal in healthy tissues,

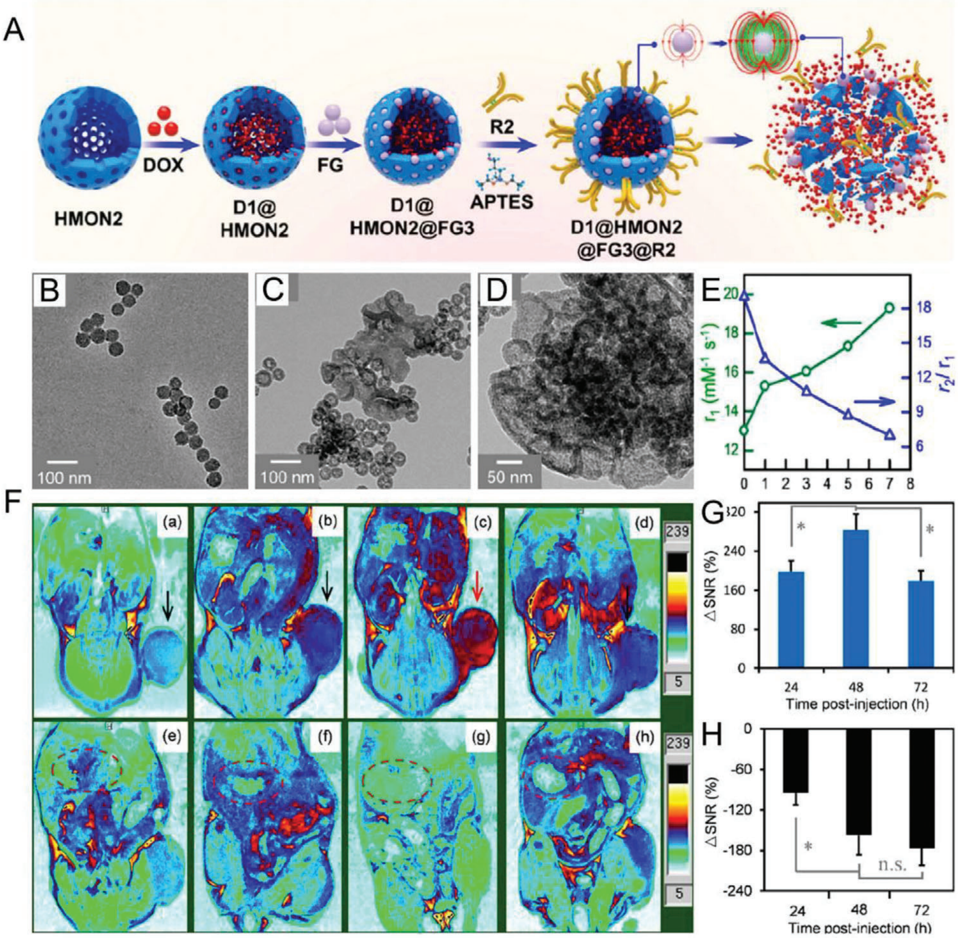

Figure 13. A) Scheme for the construction of D1@HMON2@FG3@R2 for GSH-responsive HMON degradation for 0 (B), 3 (C), and 7 (D) days. E) Change of r_1 or r_2/r_1 as a function of the incubation time in the 7.0 T magnetic field. F) MR images of U87MG tumor-bearing mice showing tumors before and after intravenous injection of D1@HMON2@FG3@R2. Quantitative analysis of the tumors (G) or livers (H) after intravenous injection of D1@HMON2@FG3@R2 using ΔSNR. Reproduced with permission.[101] Copyright 2021, American Chemical Society.

but demonstrate contrasting signals in diseased tissues.

Shen et al. developed hybrid nanoparticles consisting of a core/shell structure with dotted Fe_3O_4/Gd_2O_3 (FG) as gatekeepers, effectively blocking the pores of hollow mesoporous organosilica (HMON) nanoparticles. Furthermore, the active tumor-targeted delivery of doxorubicin hydrochloride (DOX)-loaded HMON with FG capping (D@HMON@FG@R2) was achieved by conjugating RGD dimer (R2) onto the nanoparticles, as illustrated in **Figure 13**A–D. The high r_2 value (253.7 mM^{-1} s^{-1}) and high r_2/r_1 ratio (19.13) of the aggregated FG in D@HMON@FG@R2 could lead to darkening of the normal tissue, while the intratumorally released FG resulting from GSH-triggered HMON degradation could brighten the tumors. This effect is attributed to the high r_1 value (20.1 mM^{-1} s^{-1}) and low r_2/r_1 ratio (7.01), which collectively contribute to CC-MRI (Figure 13E–H).

Moreover, Shen et al. developed a dual-responsive contrast agent (CA) for the tumor microenvironment (TME) known as SA-FeGdNP-DOX@mPEG. This CA exhibits minimal responsiveness under normal physiological conditions, but shows high responsiveness specifically to the acidic and reductive conditions found within the TME (**Figure 14**A,B). Under normal physiological environment, the SA-FeGdNP-DOX@mPEG exhibits a negative MRI signal, primarily attributed to its high r_2 value (336.9 mM^{-1} s^{-1}) and high r_2/r_1 ratio (18.4). However, within the tumor microenvironment (TME), it undergoes a switch to a positive MRI signal. This change is primarily due to the high r_1 value (20.32 mM^{-1} s^{-1}) and low r_2/r_1 ratio (7.2) associated with the SA-FeGdNP-DOX@mPEG in the TME (Figure 14C). By employing the TME dual-responsive SA-FeGdNP-DOX@mPEG, the technique of contrast-controlled magnetic resonance imaging (CC-MRI) was successfully implemented. This approach resulted in a substantial enhancement of the contrast in MR images between tumors and livers, with a remarkable ΔSNR difference of 501%.[102]

6. MRI-Guided Cancer Therapy Utilizing ES-MIONs

In the realm of precision medicine applications, the integration of therapeutic and diagnostic components within nanoplatforms, commonly referred to as theranostic elements, plays a vital role.

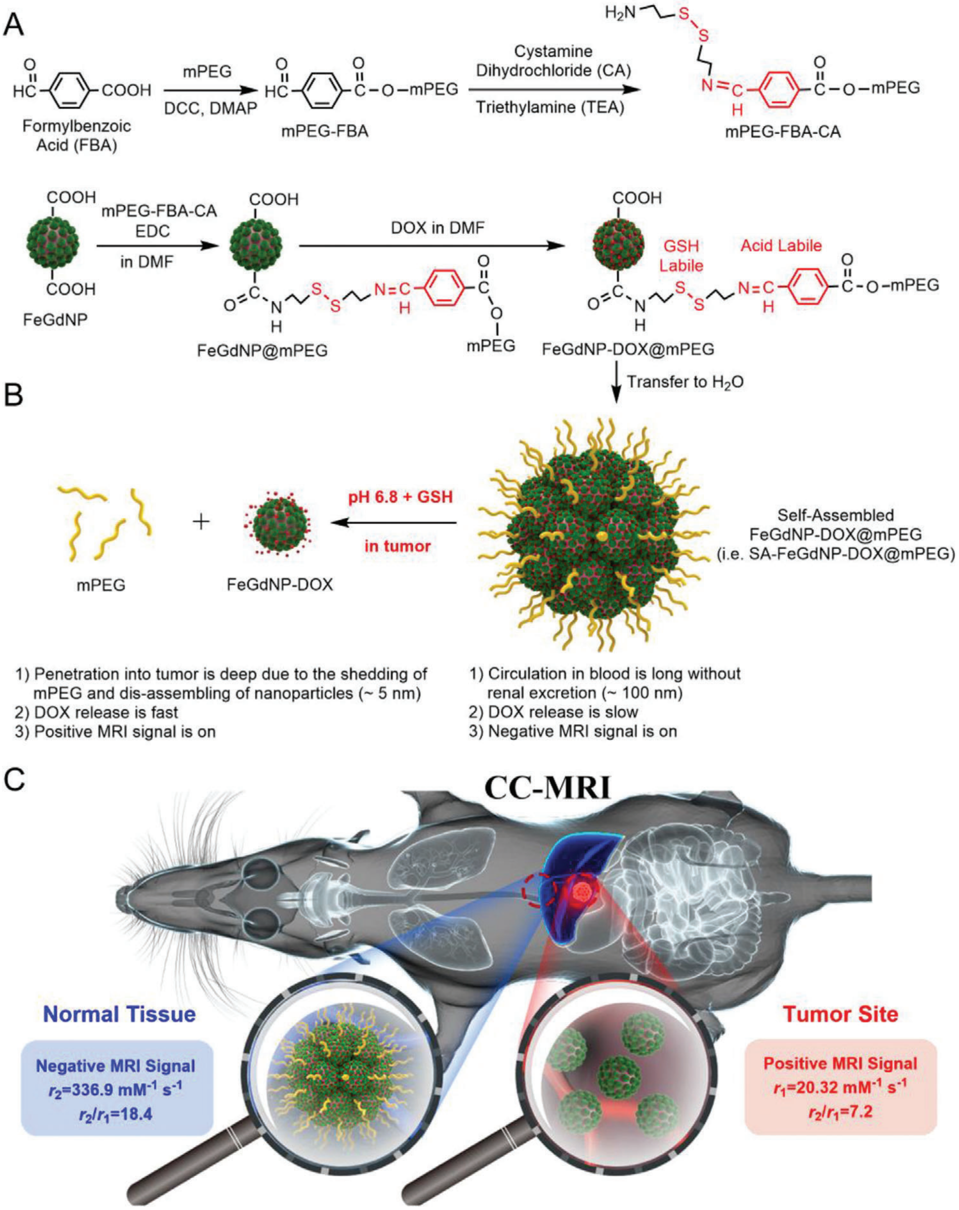

Figure 14. A) Schematic illustration of the synthesis of mPEG-FBA-CA and the CC-MRI CA. B) The self-assembled process of FeGdNP-DOX@mPEG. C) Schematic illustration of the CC-MRI of tumors using our SA-FeGdNP-DOX@mPEG. Reproduced with permission.[102] Copyright 2022, Royal Society of Chemistry.

Over the past few years, a diverse array of theranostic systems has emerged, specifically designed for imaging-guided cancer therapy. Among them, ES-MIONs have been widely developed for MRI-guided cancer therapy. For instance, ES-MIONs have proven effective in addressing the disadvantages of traditional chemotherapy, ferroptosis therapy (FT), photothermal therapy (PTT), photodynamic therapy (PDT), immunotherapy, and so on.

6.1. MRI-Guided Chemotherapy Based on ES-MIONs

In the field of nanomedicine, the integration of chemotherapy drugs with imaging agents has emerged as a prominent focus. This approach holds significant potential for advancing cancer treatment by enabling the monitoring of chemotherapy drug release, distribution, activity, and the evaluation of therapeutic effectiveness.[103]

Liu et al. developed polymersome nanovesicle encapsulating the anti-cancer drug DOX and ES-MIONs, as shown in **Figure 15**A. The obtained nanovesicles exhibited a distinctive yolk-shell structure (Figure 15B,C), characterized by controlled drug activity and suppressed T_1 MRI contrast ability. Upon reaching the tumor site, the nanovesicle exhibits a simultaneous response to glutathione (GSH), resulting in the release of the drug and activation of T_1 contrast.[104]

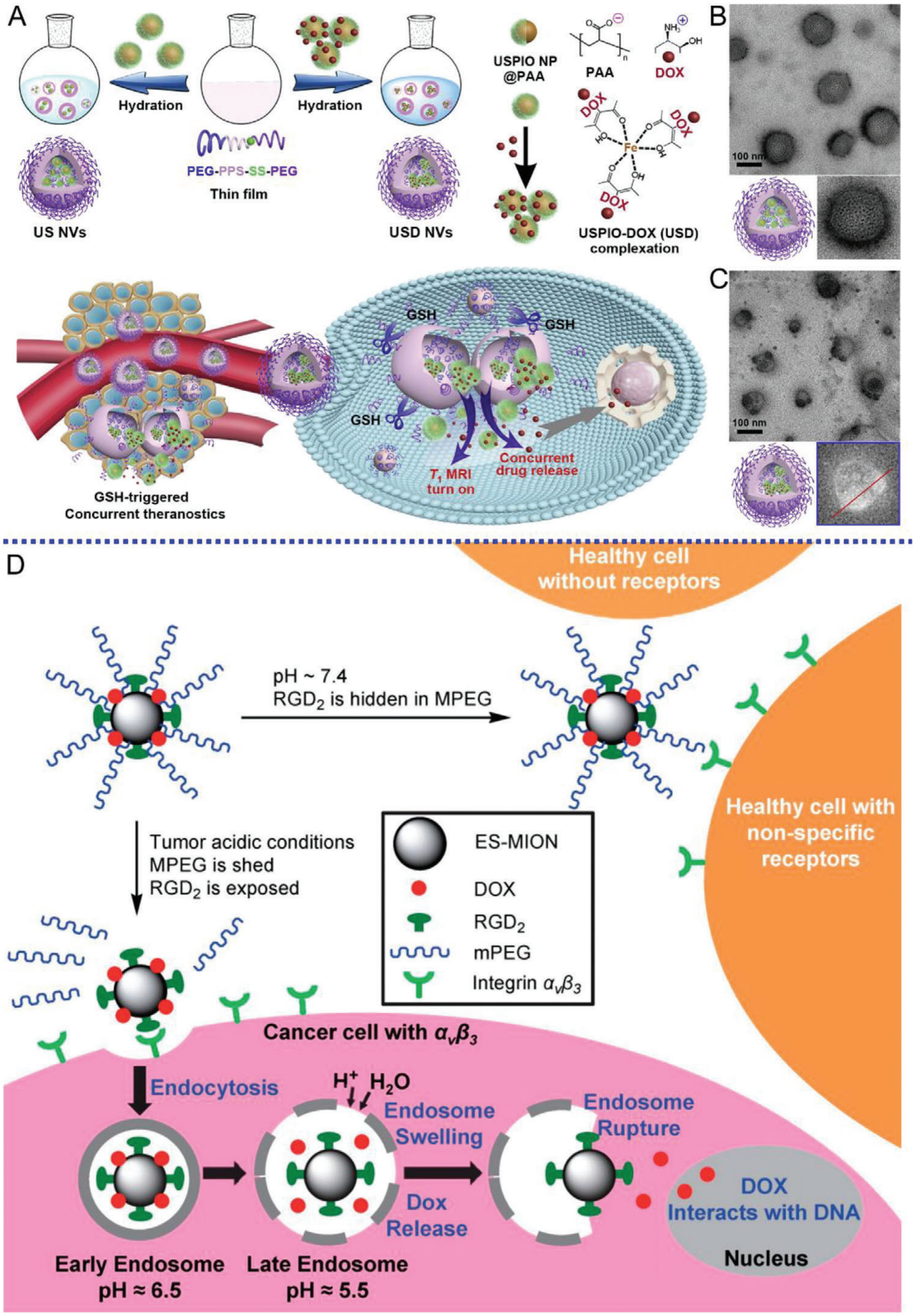

Figure 15. A) PAA-coated ES-MIONs interact with doxorubicin forming the GSH-sensitivity nanovesicles (NVs). TEM image, high-resolution TEM image (lower right) and cartoon (lower left) of B) US NVs and C) USD NVs. Reproduced with permission.[104] Copyright 2020, Elsevier. D) Design of DOX@ES-MION@RGD_2@mPEG composite nanoparticles. Reproduced with permission.[105] Copyright 2017, American Chemical Society.

Shen et al. developed a nanoplatform utilizing 3.6 nm ES-MIONs for T_1-weighted MRI CAs. The surface of ES-MIONs was modified by conjugating dimeric RGD peptide (RGD2) through the formation of amide bonds. Subsequently, DOX was loaded onto the ES-MIONs by employing hydrogen bonds, ionic bonds, and/or coordination bonds, resulting in the formation of the DOX-loaded nanoplatform. During circulation in the bloodstream, mPEG acts as a protective shield, preventing the non-specific coupling of RGD2 to healthy cells with irrelevant receptors. This is achieved by concealing RGD2 within the mPEG stealth. Nevertheless, in the presence of a mild acidic tumor environment, the acid-labile β-thiopropionate linker undergoes cleavage, leading to the detachment of mPEG from the nanoplatform. Consequently, the previously concealed RGD2

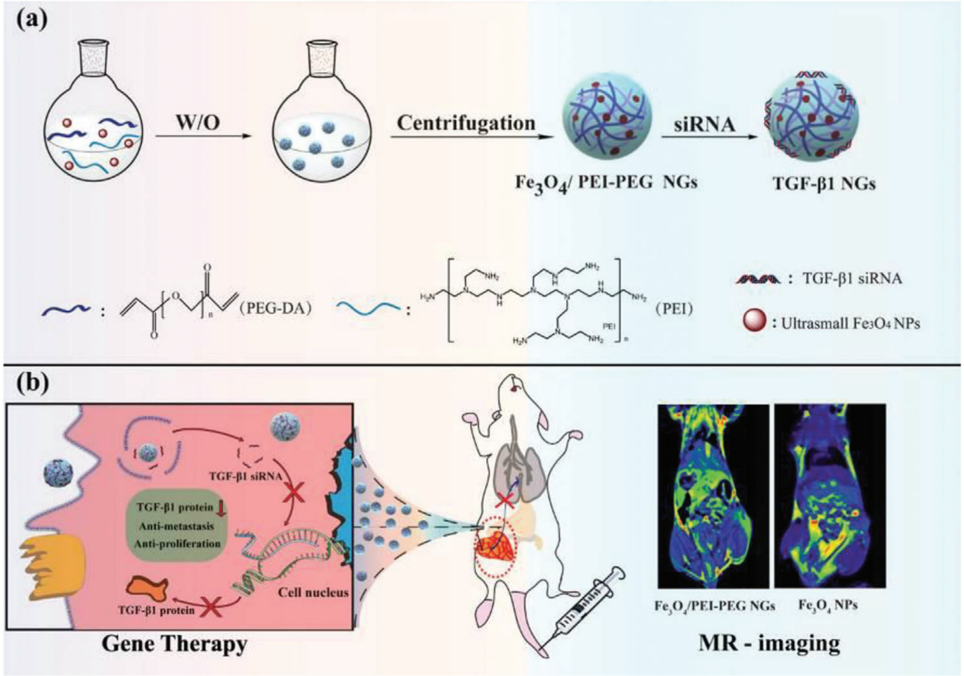

Figure 16. Schematic illustration of a) the synthesis of Fe_3O_4/PEI-PEG NGs and TGF-β1 and b) its mechanism for gene therapy and MR imaging in a mouse sarcoma model. Reproduced with permission.[106] Copyright 2021, American Chemical Society.

becomes exposed and subsequently binds to $\alpha v\beta 3$-expressing cancer cells (Figure 15D). Furthermore, the tumor imaging efficiency (ΔSNR) of this nano-platform reaches 203.4% at 12 h after injection, significantly surpassing that of the commercial Magnevist, which only achieves 55.9% at 1 h post-injection.[105]

6.2. MRI-Guided Genetherapy Based on ES-MIONs

Cao et al. described the synthesis of a nano-hydrogel composed of low-molecular-weight poly(ethylenimine) (PEI) and PEG, which was loaded with transforming growth factor-β1 (TGF-β1) siRNA and ES-MIONs (Fe_3O_4 NPs). This innovative formulation was utilized for gene therapy and T_1-weighted MRI of tumor metastasis (**Figure 16**). In the study, the formation of a nano-platform measuring 76.3 nm in size was achieved by combining sodium citrate-coated ES-MIONs, PEI, and PEG-diacrylate using an inverse microemulsion technique. The developed nano-platform display good cytocompatibility and MRI performance (r_1 = 1.0346 $\text{mM}^{-1}\ \text{s}^{-1}$). The nano-platform effectively condensed TGF-β1 siRNA through electrostatic interactions and successfully transported the siRNA to cancer cells, leading to the silencing of the TGF-β1 gene.[106]

6.3. MRI-Guided Ferroptosis Therapy Based on ES-MIONs

Ferroptosis, a mode of programmed cell death reliant on iron and reactive oxygen species (ROS), has emerged as a propitious strategy for cancer therapy.[107] Ferroptosis stands apart from apoptosis, necrosis, and autophagy by virtue of its reliance on iron and the disruption of oxidation/reduction equilibrium.[108] Furthermore, this endogenous and direct chemical energy conversion strategy operates without the need for external energy sources such as laser, ultrasound, or magnetic fields. Consequently, it overcomes the limitations associated with low tissue-penetration depth and the non-specificity of these external triggers in inducing cancer cell death.[109]

Huan et al. reported a new porous yolk-shell nano-platform with Fe_3O_4 served as the shell, and 5 nm of Fe(0) served as the core (**Figure 17**A,B). Fe(0) core was protected against oxidation by the porous Fe_3O_4 shell in the normal physiological condition. Within the acidic tumor microenvironment (TME), the pore undergoes etching, leading to the generation of fractures and subsequent exposure of Fe(0). The Fe(0) then catalyzed the ROS production and ferroptosis to cause tumor cells death. This porous yolk-shell Fe_3O_4 nano-platform has been demonstrated to be renal clearable, and effective on tumor inhibition via intravenous injection into HepG2 tumor-bearing mice.[110]

Gao et al. developed an “all-inorganic nanosystem” that does not rely on toxic chemical drugs for effective nanocatalytic tumor therapy. This system operates through a cascade catalytic reaction triggered by nanozymes, which respond to the tumor microenvironment (TME). (Figure 17C). Ultrasmall gold nanoparticles (AuNPs, diameter ≈ 1.5 nm) and Fe_3O_4NPs (diameter ≈ 1.5 nm) were successively integrated into the large pore channels of dendritic mesoporous silica nanoparticles. In this nanoplatform (Figure 17D–G), AuNPs were employed as glucose oxidase (GOx) mimics to increase the intratumoral H_2O_2 levels. Furthermore, iron oxide nanoparticles (Fe_3O_4 NPs) measuring 1.5 nm in size were employed as peroxidase mimics to catalyze the conversion of H_2O_2 into highly toxic hydroxyl radicals. This process

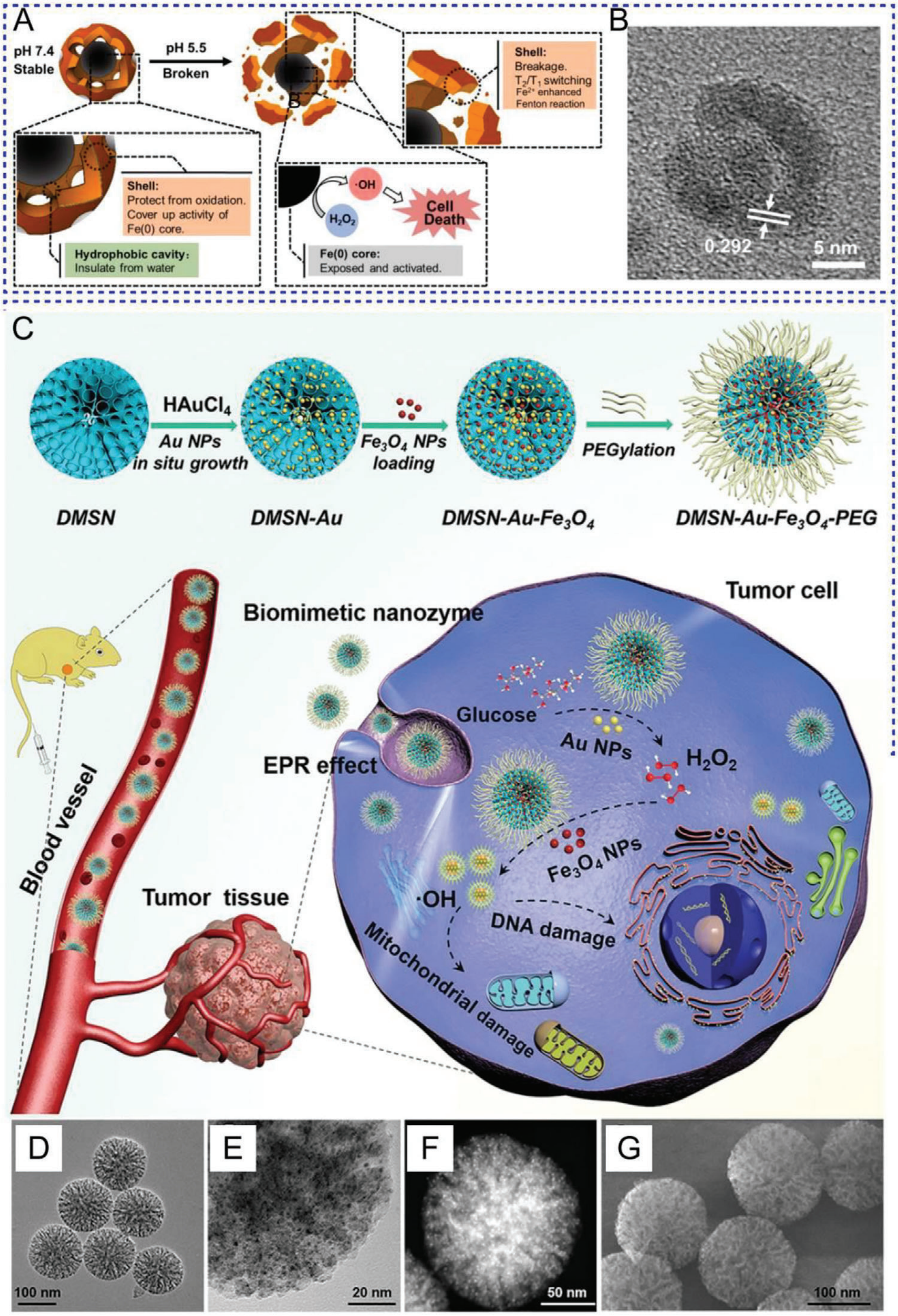

Figure 17. A) Schematic illustration of the pH activated Fe release of PYSNPs for Fenton reaction and B) HRTEM of porous yolk shell Fe/Fe_3O_4 NPs preparation. Reproduced with permission.[110] Copyright 2021, Elsevier. C) Schematic illustration of "toxic-drug-free" nanocatalytic tumor therapy by biomimetic inorganic nanomedicine-triggered cascade catalytic Fenton reaction. D,E) different magnifications, F) HADDF image, and G) SEM image of DMSN-Au-Fe_3O_4 NPs. Reproduced with permission.[111] Copyright 2019, Wiley-VCH.

triggers tumor cell death through the conventional Fenton-based catalytic reaction.[111]

Shen et al. developed a hybrid nanoplatform called cisplatin-loaded Fe_3O_4/Gd_2O_3 (FeGdNP), which was conjugated with lactoferrin (LF) and RGD peptide dimer (RGD2). This nanoplatform was designed for orthotopic tumor therapy, aiming to enhance the local concentrations of Fe^{2+} ions, Fe^{3+} ions, and H_2O_2 (**Figure 18**A). Due to LF-receptor-mediated transcytosis, these nanoparticles exhibited the ability to traverse the blood–brain barrier (BBB). By utilizing integrin $\alpha v\beta 3$-mediated

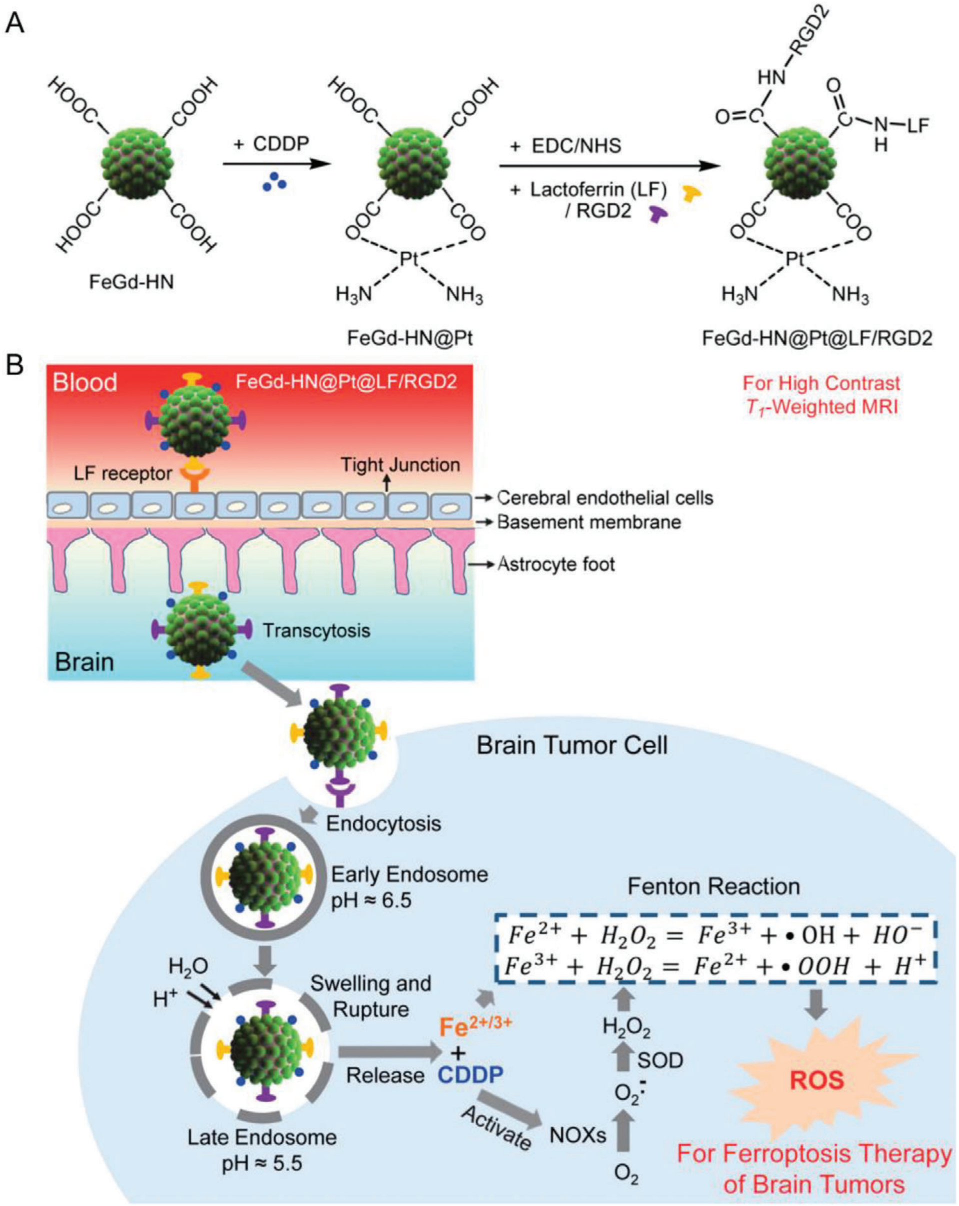

Figure 18. A) Design and synthesis of our Fenton-reaction-acceleratable magnetic nanoparticles (FeGd-HN@Pt@LF/RGD2). B) Mechanism illustration for the ferroptosis therapy (FT) of orthotopic brain tumors with self-MRI monitoring. Reproduced with permission.[112] Copyright 2018, American Chemical Society.

endocytosis, cancer cells can internalize this nanoplatform, leading to the subsequent release of Fe^{2+}, Fe^{3+}, and CDDP upon endosomal uptake and degradation. Fe^{2+} and Fe^{3+} directly engage in the Fenton reaction, while CDDP indirectly generates H_2O_2, thereby facilitating the Fenton reaction at an accelerated rate (Figure 18B). The generation of reactive oxygen species (ROS) through the accelerated Fenton reaction leads to the induction of cancer cell ferroptosis.[112]

Hu et al. utilized the strong T_1-MRI capability of FeGdNP to create a T_1-weighted magnetic resonance imaging (MRI) contrast agent. This FeGdNP was loaded with indocyanine green/glucose oxidase (ICG/GOx) and conjugated with an RGD dimer (RGD2) and an acid-labile polymer mPEG, resulting in FeGdNP-ICG/GOx-RGD2-mPEG nanoplatform. In comparison to the commercial Magnevist, the FeGdNP-ICG/GOx-RGD2-mPEG nanoplatform demonstrates a two to three-fold increase in tumor ΔSNR during MRI evaluation of peritoneal metastasis and subcutaneous animal models. Furthermore, the depletion of glucose mediated by GOx in cancer cells leads to the generation of ample gluconic acid and H_2O_2, thereby augmenting the efficiency of the Fenton reaction. The accumulation of toxic hydroxyl radicals (•OH) can impair mitochondrial function and trigger the release of reactive oxygen species from the mitochondria, subsequently activating the ferroptosis pathway.

ES-MIONs based nanoparticles have been demonstrated to release ferrous or ferric ions in acidic lysosomes, accelerating the

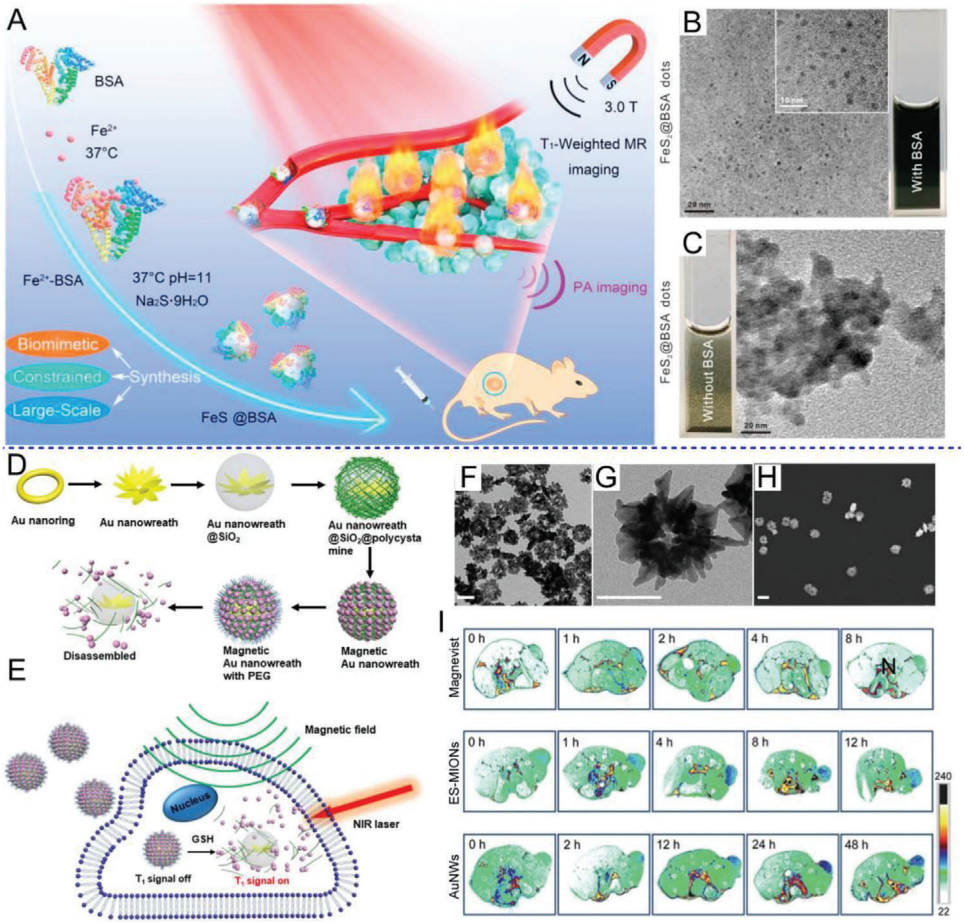

Figure 19. A) Schematic illustration of albumin-constrained biomimetic synthesis of ultrasmall-sized FeS@BSA QDs for in vivo T_1-weighted MR imaging and photo-theranostics of tumors. B) Representative TEM, HRTEM image, and a digital picture of FeS with and C) without BSA. Reproduced with permission.[45] Copyright 2020, Elsevier. D) Schematic illustration of the synthesis of magnetic gold nanowreath and E) their applications as GSH-responsive T_1-weighted imaging CAs and photothermal agents. F,G) Representative TEM images and H) SEM image of AuNWs. I) T_1-weighted images of U87MG tumor-bearing nude mice after intravenous injection of Magnevist, ES-MIONs, and magnetic AuNWs. Reproduced with permission.[118] Copyright 2018, American Chemical Society.

intracellular Fenton reaction to produce ROS. The Fenton reaction is a catalytic process that transforms hydrogen peroxide (H_2O_2) into highly hazardous reactive oxygen species (ROS), particularly hydroxyl radicals (•OH). Furthermore, iron may be the most appropriate choice for this therapeutic objective due to its biocompatibility within the human body, with a recommended daily intake for adults of ≈15 mg d^{-1}. Therefore, the targeted transport of external iron to cancerous cells is regarded as a biologically safe strategy for killing tumor cells. However, the intratumoral H_2O_2 concentration is generally 50–100 μM.[113,114] While the intratumoral H_2O_2 level is higher than that found in normal tissues and cells, it remains insufficient to generate a satisfactory and adequate quantity of •OH required to achieve desirable nano-catalytic therapeutic effectiveness through the Fenton reaction.[115] Furthermore, the lipid peroxidation (LPO) level can be relieved by the intratumoral oxidation-reduction system, resulting the inefficient ferroptosis.[116] Thus, the ES-MIONs can be designed into a composite nano drug delivery system including H_2O_2 catalyst or reducing system inhibitors.

6.4. MRI-Guided Photothermal Therapy Based on ES-MIONs

Photothermal therapy (PTT) is a non-invasive method used to treat various cancers. It relies on photoabsorbers capable of converting light energy into thermal energy, which effectively destroys cancer cells through cytotoxic heat. Nevertheless, PTT as a standalone approach for cancer treatment encounters certain challenges, such as the uneven laser energy distribution and insufficient effect in deep tumors.[117] MRI images can offer tomography information on live organisms without the constraints of penetration. Hence, combining MRI and PTT can lead to enhanced therapeutic effectiveness, reduced invasiveness, and increased cost-effectiveness.

Yang et al. developed a novel approach utilizing albumin confinement to synthesize diminutive and excellently dispersed ferrous sulfide quantum dots, referred to as FeS@BSA. (**Figure 19**A). The FeS@BSA quantum dots demonstrate an incredibly small size of approximately 3.0 nm and possess an exceptionally low magnetization (Figure 19B,C). This unique

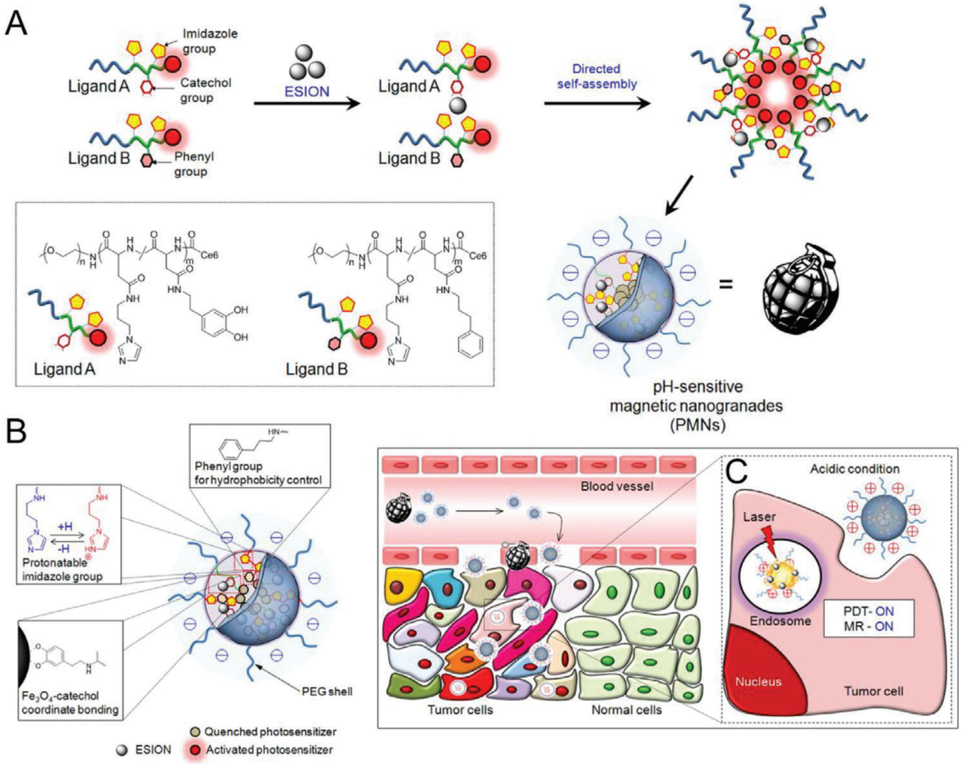

Figure 20. A) Schematic representation of pH-responsive, ligand-assisted self-assembly of ESIONs. B) pH-dependent structural transformation behavior in PMNs. C) Schematic representation of pH-dependent structural transformation and related magnetic/photoactivity change in PMNs. Reproduced with permission.[119] Copyright 2014, American Chemical Society.

characteristic grants them a desirable longitudinal relaxivity suitable for T_1-weighted MRI applications. The FeS nanoparticles demonstrate the capability to conduct MRI, exhibit enhanced absorption in the near-infrared (NIR) range, and efficiently convert the absorbed NIR light into thermal energy. FeS@BSA exhibits excellent T_1-weighted MRI capability in mice experiments, resulting in enhanced visualization of organs, blood vessels, and tumors throughout the entire body. It is intriguing that with the assistance of T_1-MRI, these ES-MIONs can be utilized for conducting photothermal therapy on tumors, leveraging their strong absorption in the near-infrared region.[45]

Liu et al. conceived a novel nanoplatform, amalgamating magnetic gold nanowreaths (AuNWs) with ES-MIONs, through the fusion of wet-chemical synthesis and layer-by-layer self-assembly approaches (Figure 19D). These AuNWs are used for visualizing tumors by T_1-weighted MRI and photoacoustic imaging to realize imaging-guided photothermal therapy (Figure 19E). In this nanoplatform based on AuNWs (Figure 19F-H), the core consists of AuNWs, exhibiting exceptional photothermal properties, while the shell is composed of an ES-MIONs assembly that can be disassembled in response to GSH. The integration of ES-MIONs enhances tumor accumulation by slowing down renal clearance and generates a GSH-responsive T_1 signal within TME (Figure 19I). With the aid of bright T_1-MRI guidance, the magnetic AuNWs exhibit a significant enhancement in photoacoustic imaging contrast within the tumor, facilitating the identification of the optimal timing for photothermal therapy intervention.[118]

6.5. MRI-Guided Photodynamic Therapy Based on ES-MIONs

Photodynamic therapy (PDT) is an approved clinical and minimally invasive treatment method for cancers that utilizes photosensitizers to generate cytotoxic singlet oxygen (SOG) upon exposure to light. However, the currently available photosensitizers lack selectivity for tumors, resulting in unintended damage to normal tissues and cells. The bioavailability, treatment efficacy, and tumor selectivity of photosensitizers can be real-time monitored by the MRI CAs, showing great potential for clinical applications.

Ling et al. developed a tumor pH-sensitive magnetic nanogrenade (PMNs) composed of ES-MIONs and pH-responsive ligands which contained chlorin e6 (Ce6) served as a photosensitizer for PDT (**Figure 20**A). The acidic tumor microenvironment (TME) triggers surface-charge switching, allowing these PMNs to effectively target tumors. Moreover, the assembled ES-MIONs undergo disassembly, activating the T_1 signal. Furthermore, the photosensitizer Ce6 exhibits self-quenching activity until it reaches the tumor site. Upon exposure to the tumor pH stimulus, this suppression is swiftly reversed, resulting in a remarkably targeted photodynamic therapy (PDT) effect (Figure 20B,C).[119]

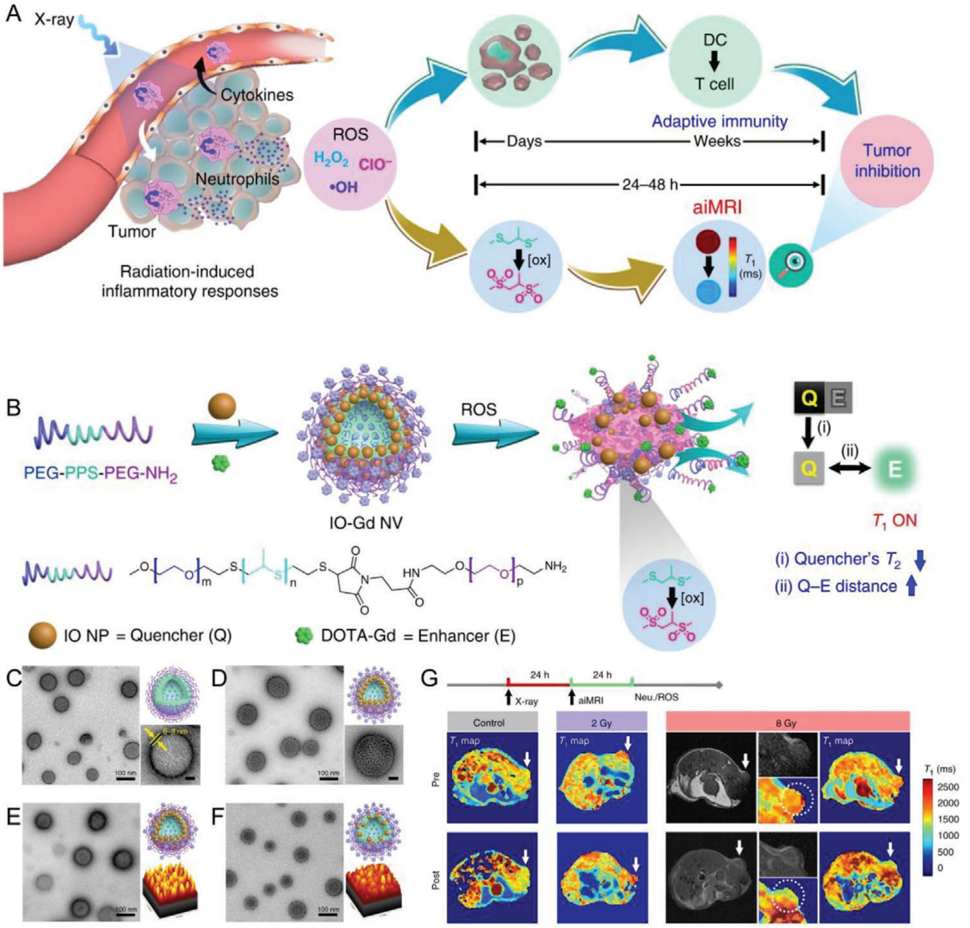

Figure 21. A) The aiMRI is applied to quantify the ROS at an early time after RT which is proposed to stratify the tumor inhibition. B) The procedure of self-assembly and disassembly of the aiMRI nanoprobe that is composed of ES-MIONs, gadolinium (Gd) species, and triblock PEG-PPS-PEG-NH$_2$ polymers. The TEM image, cartoon image (upper right), and magnified TEM image (lower right) of the blank nanoprobe with different Fe:Gd molar ratios C) blank; D) Fe:Gd = 35.5:1; E) 144:1; F) 21:1. G) The pre- and post-contrast T_1 phantom images and the quantitative T_1 relaxation maps of mouse tumors. Radiotherapy (RT) was performed 24 h prior to the aiMRI acquisition. Reproduced with permission.[120] Copyright 2020, Nature Publishing Group.

6.6. MRI-Guided Radiotherapy Based on ES-MIONs

Radiation therapy (RT), which involves the external-beam X-ray irradiation, has been widely adopted in the clinical setting for treating more than 50% of cancer patients. RT can induce DNA damage, disrupt tissue homeostasis, impair tissue resolution, cause vasculopathy, and lead to hypoxia. Regrettably, the efficacy of radiation therapy (RT) is significantly diminished as a result of the diverse radiation reactions and radioresistance exhibited across various cancer types and individuals. Consequently, there has been significant interest in the early evaluation of RT response from a biological standpoint.

Chen et al. developed an innovatively activatable inflammation magnetic resonance imaging (aiMRI) technique, aimed at the early quantitative stratification of radiation therapy (RT) response (**Figure 21**A). The inflammatory response triggered by radiation is accountable for the infiltration of neutrophils and the generation of ROS (Figure 21B). These nanovesicles were incorporated with ES-MIONs within the membrane and gadolinium (Gd) species on the surface (Figure 21C–F). The self-assembly and disassembly of the nanovesicle contribute to the dual enhancement factors in achieving a T_1 OFF-ON effect, primarily influenced by the quencher's T_2 effect and the distance between the quencher and the emitter (Q-E distance) (Figure 21G). Significant Pearson correlation coefficients (R values) are observed when examining the relationships between the changes in T_1 relaxation time within the 24–48 h timeframe following various treatments. Moreover, the aiMRI method offers a non-invasive imaging technique for early prediction of therapeutic outcomes in radiotherapy. This assists in optimizing radiation treatment planning, such as establishing delivery paths and dosages, resulting in reduced side effects and enhanced treatment outcomes.[120]

6.7. MRI-Guided Immuotherapy Based on ES-MIONs

The ES-MIONs can be applied in cancer immunotherapy because they can be used as MRI CAs, nanocarriers, and potential

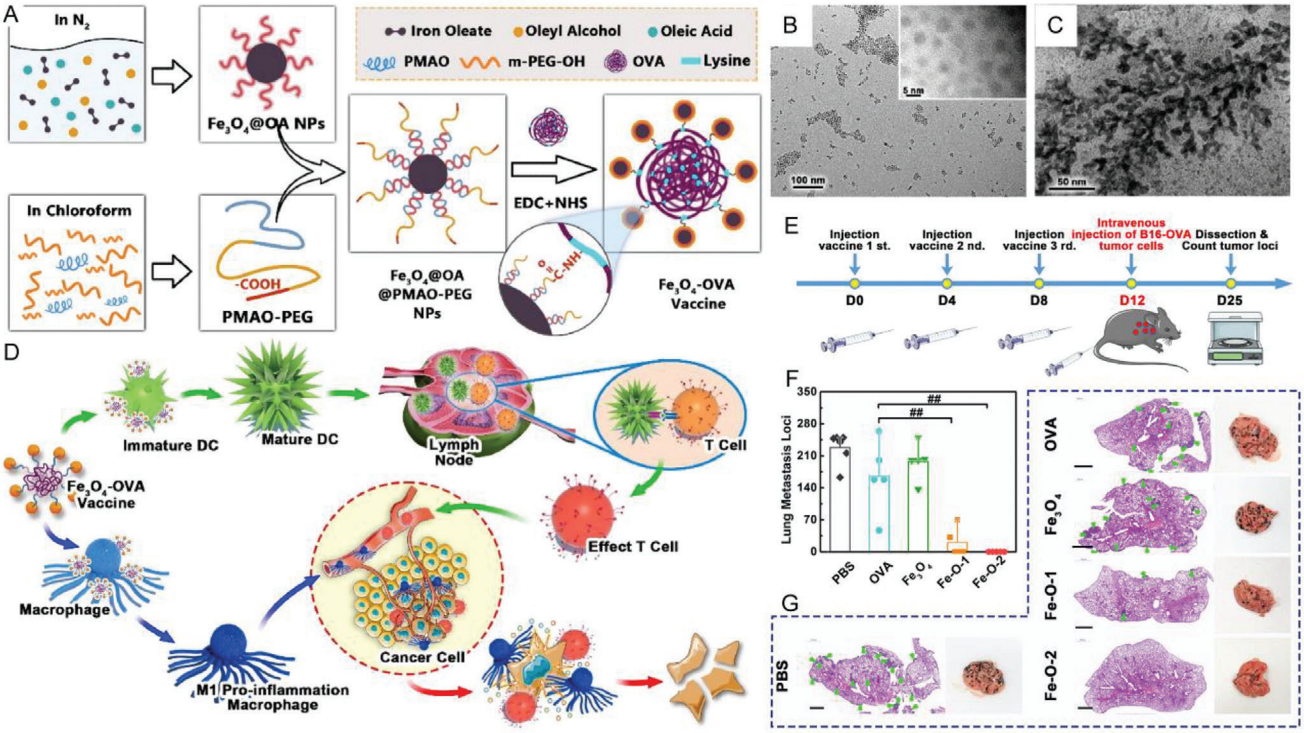

Figure 22. A) The schematic illustration on Fe_3O_4-OVA vaccine strategy. B) Schematic representation the synthesis of the Fe_3O_4-OVA vaccine. C) TEM images of Fe_3O_4 NPs and D) Fe_3O_4-OVA nanocomposites. E) The schematic experimental process of lung metastasis of B16-OVA tumor prevention study. F) Average and individual lung metastasis loci in control and treated groups intravenously injected with B16-OVA tumor cells on day 25. G) Representative images of H&E stained lungs after receiving different treatments. Reproduced with permission.[121] Copyright 2019, Elsevier.

immune system stimulatory agents. Luo et al. prepared ovalbumin-coated ES-MIONs as a nano-immunopotentiator, facilitating effective stimulation of dendritic cell-based immunotherapy and potentially activating macrophages (**Figure 22**A–C). The ovalbumin-coated ES-MIONs effectively induced the maturation of dendritic cells derived from bone marrow and promoted the release of interferon-γ (IFN-γ) from T cells. Furthermore, they have the potential to activate macrophages, leading to a significant release of tumor necrosis factor-α (Figure 22D). This therapeutic and prophylactic vaccine, incorporating ovalbumin-coated ES-MIONs, not only effectively impedes the growth of subcutaneous and metastatic B16-OVA tumors, but also demonstrates a remarkable ability to prevent the formation of both subcutaneous and metastatic tumors (Figure 22F,G). As a result, it offers a promising approach to broaden the clinical application of iron-based nanomaterials.[121]

6.8. MRI-Guided Sonodynamic Therapy Based on ES-MIONs

Sonodynamic therapy (SDT) has emerged as a cutting-edge non-invasive therapeutic modality that harnesses the power of ultrasound (US) irradiation to induce the generation of ROS through the activation of sonosensitizers. This innovative approach offers the advantage of deep tissue penetration, making it a highly desirable option for cancer therapy. Among the various sonosensitizers employed in SDT, titanium oxide (TiO2) nanomaterials are particularly noteworthy due to their exceptional chemical stability and minimal phototoxicity.

Bai et al. successfully synthesized Fe-doped titanium dioxide nanodots (Fe-TiO_2 NDs) measuring ≈2.49 nm in size, serving as a nano-platform to bolster the efficacy of SDT (**Figure 23**A). Uniform Fe-TiO2 NDs with ultrasmall size were synthesized through a simple thermal decomposition strategy, and they demonstrate well physiological stability and biocompatibility after PEGylation (Figure 23B,C). The achieved nano-platform exhibits a significantly enhanced sonodynamic effect in comparison to pure TiO_2 nanodots under ultrasonic stimulation, likely attributable to the reduction of TiO_2's band gap through the introduction of Fe dopants. Simultaneously, the presence of iron in these Fe-TiO_2-PEG nanodots enables the triggering of a Fenton reaction using H_2O_2, leading to the generation ROS. This capability facilitates chemodynamic therapy as it directly induces the destruction of tumor cells (Figure 23D). The incorporation of iron ions also imparts T_1-MRI capability to the Fe-TiO_2 nanodots, with an approximate r_1 value of 4.71 mM^{-1} s^{-1}. Additionally, a significant proportion of the ultrasmall Fe-TiO_2 nanodots can be efficiently eliminated from the body within a month, thereby exhibiting no discernible long-term toxicity in the treated mice.[122]

6.9. Multimode Imaging-Guided Therapy Based on ES-MIONs

The utilization of multimodal contrast agents holds great promise in facilitating tumor therapy and minimizing the

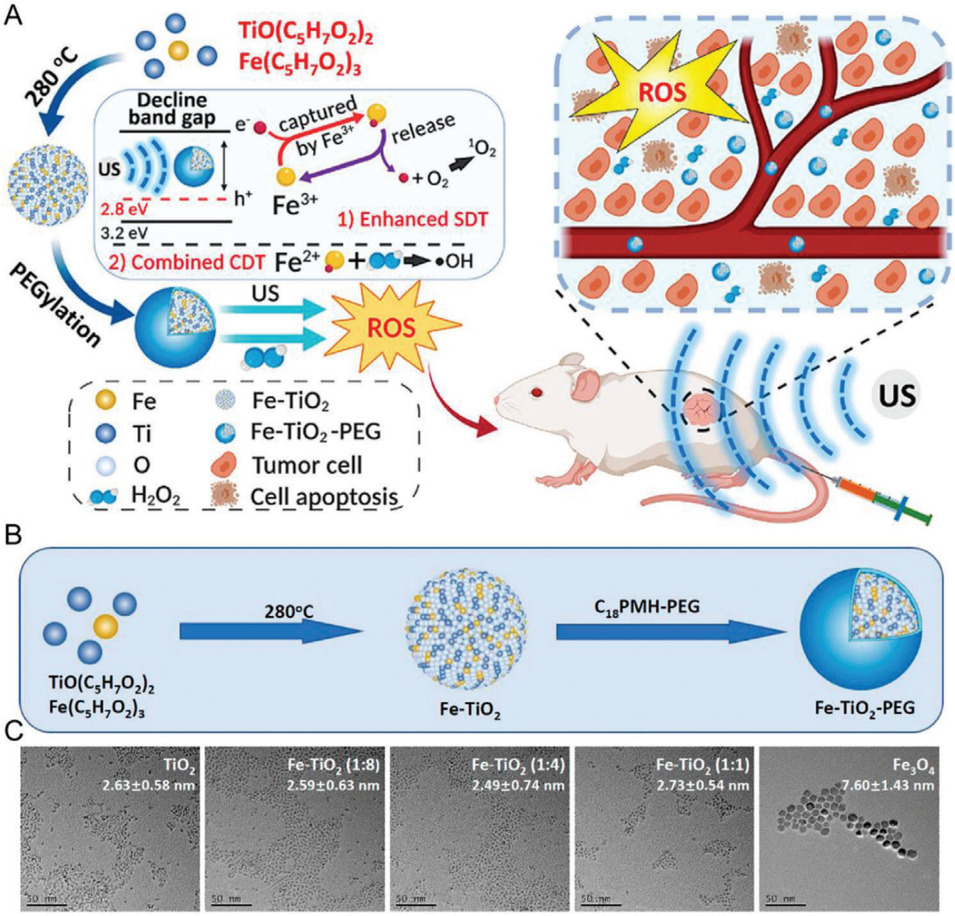

Figure 23. A) Ultrasmall Fe-TiO_2 NDs were synthesized via the thermal decomposition of metal-organic precursors. The synthesized Fe-TiO_2 NDs showed enhanced sonodynamic and chemodynamic effects for dual-modal imaging-guided SDT/CDT combined therapy due to the Fe doping. B) Illustration of the preparation process of Fe-TiO_2 NDs. C) TEM images of pure TiO_2, Fe_3O_4, and Fe-TiO_2 NDs with different feeding ratios obtained via a similar method. Reproduced with permission.[122] Copyright 2020, American Chemical Society.

deleterious impact on neighboring healthy tissues throughout the cancer treatment process. The multimode imaging-guided therapy based on ES-MIONs has been developed with enhanced diagnostic sensitivity and therapeutic efficacy.

Lu et al. introduced a straightforward methodology for the synthesis of dendrimer-stabilized Au nanoflowers that incorporate ES-MIONs, enabling multimode imaging-guided tumor combination therapy (**Figure 24**A). In this study, the researchers initially synthesized generation 5 (G5) poly(amidoamine) dendrimer-stabilized gold nanoparticles (AuNPs) and citrate-stabilized ES-MIONs (with a diameter of 2.1 nm). The synthesis of these nanoparticles was achieved through the self-reduction and hydrothermal methods, respectively. Subsequently, the seed particles, which comprised both AuNPs and ES-MIONs, were employed to produce Au nanoflowers using a seed-mediated approach (Figure 24B,C). The resultant dendrimer-stabilized ES-MIONs/Au nanoflowers exhibit a remarkable r_1 value of 3.22 mM^{-1} s^{-1}, along with an impressive photothermal conversion efficiency of 82.7% (Figure 24D). These properties enable the utilization of multimode T_1-MRI/CT/PA imaging for effective guidance in PTT therapy and RT treatment of tumors, resulting in enhanced therapeutic outcomes (Figure 24E, F).[123]

Cui et al. prepared a sophisticated multifunctional nanoplatform for integrated diagnosis and treatment, which combined ES-MIONs, MnO2, photosensitive drugs, and traditional Chinese medicine monomers into a cohesive system (**Figure 25**A). Within the nanoplatform, a layer of MnO_2 was strategically grown onto the ES-MIONs (Figure 25B,C), complemented by the subsequent loading of Ce6 and CSL through electrostatic interactions. Benefiting from the enhanced EPR effect, the nanoplatform exhibits remarkable accumulation within tumor tissues. Notably, the outer layer of the nanoplatform, consisting of MnO_2, facilitates the efficient decomposition of H_2O_2 into O_2, thereby ameliorating tumor hypoxia and augmenting the PDT efficacy of Ce6. Simultaneously, within the acidic tumor microenvironment (TME), the rapid degradation of MnO_2 within the nanoplatform triggers the selective liberation of the encapsulated drugs, Mn^{2+}, and ES-MIONs. This orchestrated release mechanism not only intensifies the drug accumulation specifically within tumor sites but also amplifies the T_1/T_2 contrast during fluorescence (Figure 25D) and MRI (Figure 25E,F) imaging.[124]

Wang et al. synthesized a facile Fe-based core–shell nanoplatform with enhanced CDT and multiple functions for cancer therapy (**Figure 26**A). This nanoplatform was constructed by

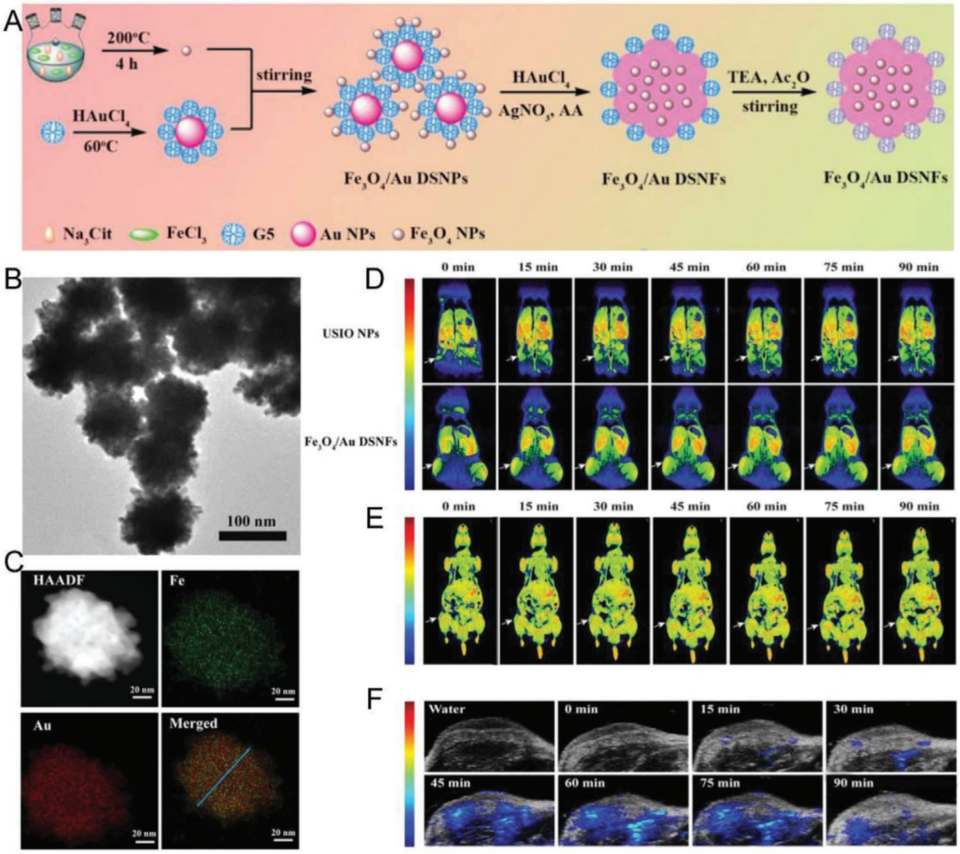

Figure 24. A) Schematic illustration of the preparation of the Fe_3O_4/Au nanoplatform for multimode imaging-guided combination therapy of tumors. B) TEM images and C) element mapping of Fe_3O_4/Au nanoplatform. D) In vivo T_1-weighted MR images. E) CT images and F) PA images of the 4T1 tumor in nude mice by injection of the Fe_3O_4/Au nanoplatform under 808 nm laser irradiation. Reproduced with permission.[123] Copyright 2018, Wiley-VCH.

redox self-assembly strategy with Fe_xO_y served as the shell, and noble metal (Au, or Pd) served as the core. Remarkably, the Fe_xO_y shell can be effectively triggered by a minimal quantity of $NaBH_4$, leading to a significant amplification of •OH production during subsequent Fenton reactions. Additionally, the nanoplatform exhibits a favorable photothermal effect, which further facilitates the generation of •OH. Thus, under the guidance of pH-responsive T_1-weighted MRI (Figure 26B), CT imaging (Figure 26C), and thermal imaging (Figure 26D), this nanoplatform achieved synergetic PTT and Fenton-related CDT therapy for cancer.[125]

7. Conclusions and Future Perspective

ES-MIONs have been developed as a novel T_1-MRI CA with good biocompatibility, and have become a potential MRI-guided therapeutic agent for tumor theranostics. With the particle size less than 5 nm, the ES-MIONs provide a high number of surface-exposed ferric ions for water proton coordination and chemical exchange, showing a T_1 relaxation enhancement effect. More importantly, the ES-MIONs can be perfectly integrated into nanoplatforms that can guide various tumor treatments, including chemotherapy, gene therapy, FT, PTT, PDT, RT, immunotherapy, and so on. Combined therapies based on ES-MIONs achieve more excellent anti-tumor effects. In this review, we have introduced the current T_1-MRI CAs, the preparation and surface modification methods of ES-MIONs, the enhancement strategies for ES-MIONs-based T_1-MRI, and MRI-guided cancer therapy utilizing ES-MIONs. Nonetheless, the utilization of ES-MIONs-based nanomaterials in the domain of tumor theranostics remains at its rudimentary stage of exploration and advancement, with a multitude of predicaments and obstacles yet to be resolved.

First, the stable blood circulation after intravenous injection is directly related to the clinical MRI efficiency. For MRI purpose, the ES-MIONs should quickly reach the tumors, usually less than 2 h. While for the imaing-guided tumor therapy, longer time is necessary to obtain high accumulation of ES-MIONs in tumors and enhanced therapeutic efficacy. In addition, too long circulation time is inconvenient for patient to wait for the best MRI scanning window, which further hinder the clinical application of ES-MIONs.

Second, the tumor accumulation efficiency of ES-MIONs is required more in-depth exploration. Although targeting ligands could be grafted onto ESMIONs surface to promote tumor accumulation via active binding to the overexpressed biomarker of tumors, it also could be hindered by the mask of protein corona layer on the ESMIONs surface, and the insufficient expression of receptor.

Third, the biosafety and long-term toxicity should be investigated in detail for the application of ES-MIONs in vivo. Although

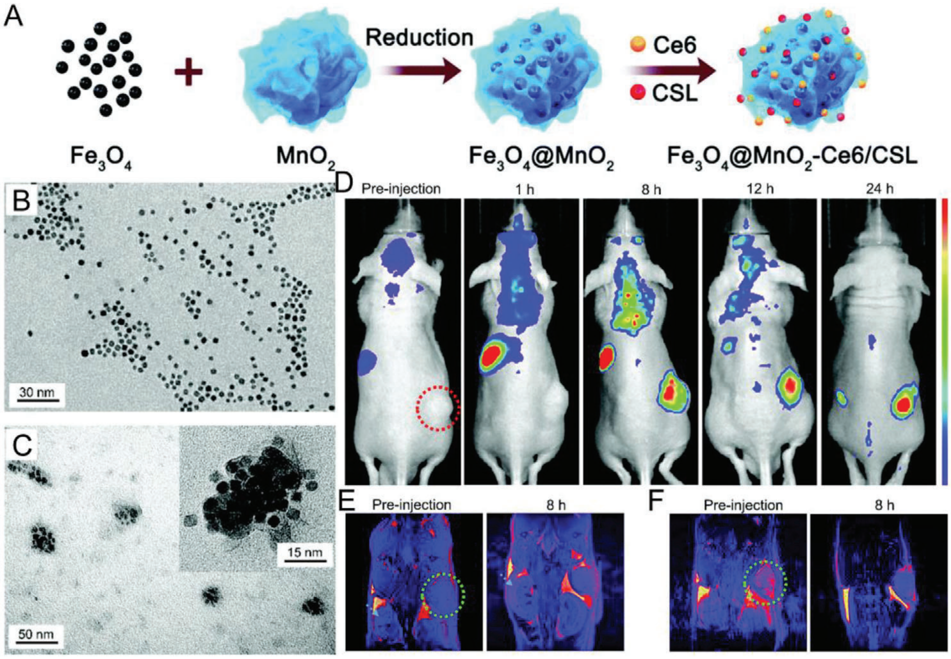

Figure 25. A) Schematic illustration of the synthetic process of $Fe_3O_4@MnO_2$-Ce6/CSL and mechanism of cellular uptake process and pH/H_2O_2-triggered MRI/FL imaging and CT/PDT combination treatment. B) TEM images of Fe_3O_4 NCs and C) $Fe_3O_4@MnO_2$-Ce6/CSL. D) In vivo real-time fluorescence imaging, E) T_1-weighted MR images, and F) T_2 -weighted MR images of tumor-bearing mice by injection of $Fe_3O_4@MnO_2$-Ce6/CSL. Reproduced with permission.[124] Copyright 2021, Royal Society of Chemistry.

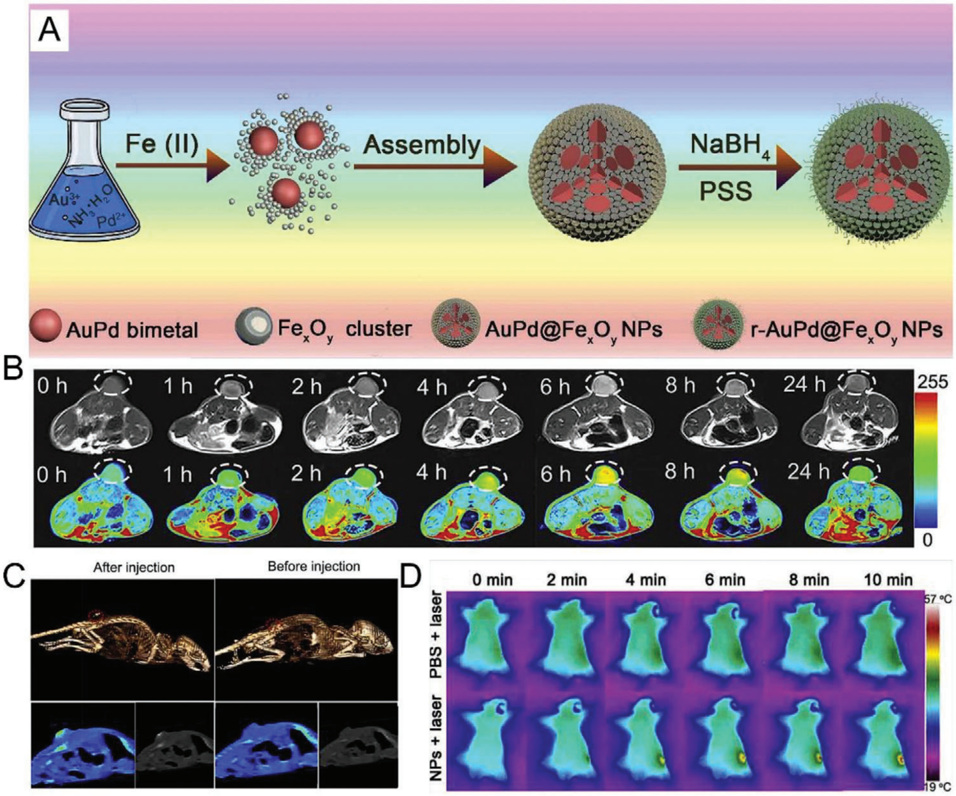

Figure 26. A) Schematic illustration of the synthetic process of r-AuPd@Fe_xO_y NPs and application of r-AuPd@Fe_xO_y NPs for oncotherapy. B) In vivo T_1-MRI and C) CT images of tumor-bearing mice after the intratumoral injection of r-AuPd@Fe_xO_y NPs. D) Thermal images of A549 tumor-bearing mice with PBS or AuPd@AuPd@Fe_xO_y NPs treatment. Reproduced with permission.[125] Copyright 2021, Elsevier.

the reported ES-MIONs caused no damage to the normal tissues and organs and can be rapidly eliminated away from the body via kidney, a more thorough and extended evaluation of their biosafety is necessary, especially on larger animal models.

Furthermore, the preparation methods are the key factor affecting the efficacy of nanomaterials. The ES-MIONs is more likely to retention in tumor tissue when it has a high hydrophilicity and mono-dispersity in aqueous solutions. However, the ES-MIONs prepared by the thermal decomposition method have worse dispersibility in aqueous solutions with or without adequate hydrophilic ligand exchange. Therefore, more functional ligands should be further exploited to enable the ES-MIONs to be stable in physiological solution without aggregation. In addition, it is also crucial to keep the size homogenization of ES-MIONs during the storage period.

Finally, ES-MIONs exhibit promising prospects for diverse therapeutic modalities. However, their in vivo biological degradability necessitates further comprehensive investigation. In the reported studies, ES-MIONs based nanomaterials were mainly used in chemotherapy, ferroptosis therapy, photothermal and photodynamic therapy, but their application in gene therapy, radiotherapy, immunotherapy, and sondynamic therapy is rarely reported. Hence, it is imperative to foster greater innovation in exploring the applications of ES-MIONs across a diverse range of therapeutic modalities.

Though there are remaining some issues to be addressed, ES-MIONs have emerged as a promising new tool for the diagnosis and treatment of cancer. Its application is worth further development and exploration. We believe that the ES-MIONs based nanomedicine has a good development prospect and will become a choice for cancer patients.

Acknowledgements

This work was financially supported by the Guangdong Provincial Natural Science Foundation of China (2021A1515010605), the Guangzhou Key Research and Development Program of China (202103000094), and the National Natural Science Foundation of China (32271374).

Conflict of Interest

The authors declare no conflict of interest.

Keywords

contrast agents (CAs), exceedingly small magnetic iron oxide nanoparticles (ES-MIONs), magnetic resonance imaging (MRI), MRI-guided cancer therapy

Received: April 5, 2023
Revised: August 1, 2023
Published online: August 18, 2023

---

[1] M. Gao, F. Yu, C. Lv, J. Choo, L. Chen, *Chem. Soc. Rev.* **2017**, *46*, 2237.
[2] M. Morrow, J. Waters, E. Morris, *Lancet* **2011**, *378*, 1804.
[3] L. M. Johnson, B. Turkbey, W. D. Figg, P. L. Choyke, *Nat. Rev. Clin. Oncol.* **2014**, *11*, 346.
[4] G. L. Davies, I. Kramberger, J. J. Davis, *Chem. Commun.* **2013**, *49*, 9704.
[5] S. R. Zhang, M. Merritt, D. E. Woessner, R. E. Lenkinski, A. D. Sherry, *Acc. Chem. Res.* **2003**, *36*, 783.
[6] J. Wahsner, E. M. Gale, A. Rodriguez-Rodriguez, P. Caravan, *Chem. Rev.* **2019**, *119*, 957.
[7] Y. Xiang, J. Wang, *Quant Imag Med Surg* **2011**, *1*, 35.
[8] L. Gu, R. H. Fang, M. J. Sailor, J. H. Park, *ACS Nano* **2012**, *6*, 4947.
[9] H. B. Na, I. C. Song, T. Hyeon, *Adv. Mater.* **2009**, *21*, 2133.
[10] J. W. M. Bulte, D. L. Kraitchman, *NMR Biomed.* **2004**, *17*, 484.
[11] Y. Bao, J. A. Sherwood, Z. Sun, *J. Mater. Chem. C* **2018**, *6*, 1280.
[12] M. Jeon, M. V. Halbert, Z. R. Stephen, M. Zhang, *Adv. Mater.* **2021**, *33*, 1906539
[13] D. Ling, N. Lee, T. Hyeon, *Acc. Chem. Res.* **2015**, *48*, 1276.
[14] C. Chen, J. X. Ge, Y. Gao, L. Chen, J. B. Cui, J. F. Zeng, M. Y. Gao, *Wires Nanomed Nanobi* **2021**, e1740.
[15] Z. Shen, T. Chen, X. Ma, W. Ren, Z. Zhou, G. Zhu, A. Zhang, Y. Liu, J. Song, Z. Li, H. Ruan, W. Fan, L. Lin, J. Munasinghe, X. Chen, A. Wu, *ACS Nano* **2017**, *11*, 10992.
[16] M. E. Lorkowski, P. U. Atukorale, K. B. Ghaghada, E. Karathanasis, *Adv. Healthcare Mater.* **2021**, *10*, 2001044.
[17] Z. Zhou, L. Yang, J. Gao, X. Chen, *Adv. Mater.* **2019**, *31*, 1804567.
[18] Q. Liu, Y.-J. Kim, G.-B. Im, J. Zhu, Y. Wu, Y. Liu, S. H. Bhang, *Adv. Funct. Mater.* **2021**, *31*, 2008171.
[19] J. Shin, R. M. Anisur, M. K. Ko, G. H. Im, J. H. Lee, I. S. Lee, *Angew Chem Int Ed Engl* **2009**, *48*, 321.
[20] C. C. Huang, N. H. Khu, C. S. Yeh, *Biomaterials* **2010**, *31*, 4073.
[21] J. H. Youk, J. M. Lee, C. S. Kim, *Am. J. Roentgenol.* **2004**, *183*, 1049.
[22] G. Elizondo, C. J. Fretz, D. D. Stark, S. M. Rocklage, S. C. Quay, D. Worah, Y. M. Tsang, M. C. Chen, J. T. Ferrucci, *Radiology* **1991**, *178*, 73.
[23] S. Anbu, S. H. L. Hoffmann, F. Carniato, L. Kenning, T. W. Price, T. J. Prior, M. Botta, A. F. Martins, G. J. Stasiuk, *Angew. Chem., Int. Ed.* **2021**, *60*, 10736.
[24] S. Karbalaei, E. Knecht, A. Franke, A. Zahl, A. C. Saunders, P. R. Pokkuluri, R. J. Beyers, I. Ivanovic-Burmazovic, C. R. Goldsmith, *Inorg. Chem.* **2021**, *60*, 8368.
[25] J. G. Penfield, R. F. Reilly, Jr., *Nat. Clin. Pract. Nephrol.* **2007**, *3*, 654.
[26] J. Perez-Rodriguez, S. Lai, B. D. Ehst, D. M. Fine, D. A. Bluemke, *Radiology* **2009**, *250*, 371.
[27] T. Kanda, K. Ishii, H. Kawaguchi, K. Kitajima, D. Takenaka, *Radiology* **2014**, *270*, 834.
[28] T. H. Shin, Y. Choi, S. Kim, J. Cheon, *Chem. Soc. Rev.* **2015**, *44*, 4501.
[29] Y. Hou, R. Qiao, F. Fang, X. Wang, C. Dong, K. Liu, C. Liu, Z. Liu, H. Lei, F. Wang, M. Gao, *ACS Nano* **2013**, *7*, 330.
[30] C. Y. Cao, Y. Y. Shen, J. D. Wang, L. Li, G. L. Liang, *Sci. Rep.* **2013**, *3*, 1024.
[31] C. Liu, Z. Gao, J. Zeng, Y. Hou, F. Fang, Y. Li, R. Qiao, L. Shen, H. Lei, W. Yang, M. Gao, *ACS Nano* **2013**, *7*, 7227.
[32] Z. Shen, W. Fan, Z. Yang, Y. Liu, V. I. Bregadze, S. K. Mandal, B. C. Yung, L. Lin, T. Liu, W. Tang, L. Shan, Y. Liu, S. Zhu, S. Wang, W. Yang, L. H. Bryant, D. T. Nguyen, A. Wu, X. Chen, *Small* **2019**, *15*, 1903422.
[33] Z. Shen, T. Liu, Z. Yang, Z. Zhou, W. Tang, W. Fan, Y. Liu, J. Mu, L. Li, V. I. Bregadze, S. K. Mandal, A. A. Druzina, Z. Wei, X. Qiu, A. Wu, X. Chen, *Biomaterials* **2020**, *235*, 119783.
[34] Z. Wei, Z. Jiang, C. Pan, J. Xia, K. Xu, T. Xue, B. Yuan, O. U. Akakuru, C. Zhu, G. Zhang, Z. Mao, X. Qiu, A. Wu, Z. Shen, *Small* **2020**, *16*, 1906870.
[35] X. Qian, X. Han, L. Yu, T. Xu, Y. Chen, *Adv. Funct. Mater.* **2020**, *30*, 1907066.
[36] G. I. Dar, M. Z. Iqbal, O. U. Akakuru, C. Y. Yao, G. Awiaz, A. G. Wu, *J. Mater. Chem. B* **2020**, *8*, 8356.

[37] Y. Wang, Z. Cao, Q. Wei, K. Ma, W. Hu, Q. Huang, J. Su, H. Li, C. Zhang, X. Fu, *Acta Biomater.* **2022**, *147*, 342.
[38] W. Hou, Y. Jiang, G. Xie, L. Zhao, F. Zhao, X. Zhang, S.-K. Sun, C. Yu, J. Pan, *Nanoscale* **2021**, *13*, 8531.
[39] J. D. Cook, C. H. Flowers, B. S. Skikne, *Blood* **2003**, *101*, 3359.
[40] X. Lu, H. Zhou, Z. Liang, J. Feng, Y. Lu, L. Huang, X. Qiu, Y. Xu, Z. Shen, *J. Nanobiotechnol.* **2022**, *20*, 350.
[41] C. Du, X. Liu, H. Hu, H. Li, L. Yu, D. Geng, Y. Chen, J. Zhang, *J. Mater. Chem. B* **2020**, *8*, 2296.
[42] C. Du, J. Wang, X. Liu, H. Li, D. Geng, L. Yu, Y. Chen, J. Zhang, *Biomaterials* **2020**, *230*, 119581.
[43] N. Chan, M. Laprise-Pelletier, P. Chevallier, A. Bianchi, M.-A. Fortin, J. K. Oh, *Biomacromolecules* **2014**, *15*, 2146.
[44] D. Ma, J. Chen, Y. Luo, H. Wang, X. Shi, *J. Mater. Chem. B* **2017**, *5*, 7267.
[45] W. Yang, C. Xiang, Y. Xu, S. Chen, W. Zeng, K. Liu, X. Jin, X. Zhou, B. Zhang, *Biomaterials* **2020**, *255*, 120186.
[46] H. Zhang, L. Li, X. L. Liu, J. Jiao, C. T. Ng, J. B. Yi, Y. E. Luo, B. H. Bay, L. Y. Zhao, M. L. Peng, N. Gu, H. M. Fan, *ACS Nano* **2017**, *11*, 3614.
[47] S. Guo, Z. Li, J. Feng, W. Xiong, J. Yang, X. Lu, S. Yang, Y. Xu, A. Wu, Z. Shen, *Nano Today* **2022**, *47*, 101663.
[48] S. Chen, J. Yang, Z. Liang, Z. Li, W. Xiong, Q. Fan, Z. Shen, J. Liu, Y. Xu, *ACS Appl. Mater. Interfaces* **2023**, *15*, 2705.
[49] A. Ali, H. Zafar, M. Zia, I. Ul Haq, A. R. Phull, J. S. Ali, A. Hussain, *Nanotechnol Sci Appl* **2016**, *9*, 49.
[50] G. Wang, X. Zhang, A. Skallberg, Y. Liu, Z. Hu, X. Mei, K. Uvdal, *Nanoscale* **2014**, *6*, 2953.
[51] Z. Li, P. W. Yi, Q. Sun, H. Lei, H. L. Zhao, Z. H. Zhu, S. C. Smith, M. B. Lan, G. Q. Lu, *Adv. Funct. Mater.* **2012**, *22*, 2387.
[52] B. Chen, Z. Guo, C. Guo, Y. Mao, Z. Qin, D. Ye, F. Zang, Z. Lou, Z. Zhang, M. Li, Y. Liu, M. Ji, J. Sun, N. Gu, *Nanoscale* **2020**, *12*, 5521.
[53] M. O. Besenhard, L. Panariello, C. Kiefer, A. P. LaGrow, L. Storozhuk, F. Perton, S. Begin, D. Mertz, N. T. K. Thanh, A. Gavriilidis, *Nanoscale* **2021**, *13*, 8795.
[54] Y. K. Peng, C. L. Liu, H. C. Chen, S. W. Chou, W. H. Tseng, Y. J. Tseng, C. C. Kang, J. K. Hsiao, P. T. Chou, *J. Am. Chem. Soc.* **2013**, *135*, 18621.
[55] C. L. Liu, Y. K. Peng, S. W. Chou, W. H. Tseng, Y. J. Tseng, H. C. Chen, J. K. Hsiao, P. T. Chou, *Small* **2014**, *10*, 3962.
[56] H. Wei, O. T. Bruns, M. G. Kaul, E. C. Hansen, M. Barch, A. Wiśniowska, O. Chen, Y. Chen, N. Li, S. Okada, J. M. Cordero, M. Heine, C. T. Farrar, D. M. Montana, G. Adam, H. Ittrich, A. Jasanoff, P. Nielsen, M. G. Bawendi, *Proc. Natl. Acad. Sci. USA* **2017**, *114*, 2325.
[57] L. Xiao, J. Li, D. F. Brougham, E. K. Fox, N. Feliu, A. Bushmelev, A. Schmidt, N. Mertens, F. Kiessling, M. Valldor, B. Fadeel, S. Mathur, *ACS Nano* **2011**, *5*, 6315.
[58] Y. Tian, B. Yu, X. Li, K. Li, *J. Mater. Chem.* **2011**, *21*, 2476.
[59] J. Vidal-Vidal, J. Rivas, M. A. López-Quintela, *Colloids Surf., A* **2006**, *288*, 44.
[60] L. H. Shen, J. F. Bao, D. Wang, Y. X. Wang, Z. W. Chen, L. Ren, X. Zhou, X. B. Ke, M. Chen, A. Q. Yang, *Nanoscale* **2013**, *5*, 2133.
[61] J. Y. Park, P. Daksha, G. H. Lee, S. Woo, Y. Chang, *Nanotechnology* **2008**, *19*, 365603.
[62] H. Qu, D. Caruntu, H. Liu, C. J. O'Connor, *Langmuir* **2011**, *27*, 2271.
[63] T. A. Lastovina, A. P. Budnyk, S. P. Kubrin, A. V. Soldatov, *Mendeleev Commun.* **2018**, *28*, 167.
[64] R. Bhavesh, A. V. Lechuga-Vieco, J. Ruiz-Cabello, F. Herranz, *Nanomaterials* **2015**, *5*, 1880.
[65] C. Miao, F. Hu, Y. Rui, Y. Duan, H. Gu, *J. Mater. Chem. B* **2019**, *7*, 2081.
[66] M. Tadić, V. Kusigerski, D. Marković, M. Panjan, I. Milošević, V. Spasojević, *J. Alloys Compd.* **2012**, *525*, 28.
[67] Y. Cai, Y. Wang, H. Xu, C. Cao, R. Zhu, X. Tang, T. Zhang, Y. Pan, *Nanoscale* **2019**, *11*, 2644.
[68] S. Xu, J. Wang, Y. Wei, H. Zhao, T. Tao, H. Wang, Z. Wang, J. Du, H. Wang, J. Qian, K. Ma, J. Wang, *ACS Appl. Mater. Interfaces* **2020**, *12*, 56701.
[69] Y.-K. Peng, S. C. E. Tsang, P.-T. Chou, *Mater. Today* **2016**, *19*, 336.
[70] A. Hannecart, D. Stanicki, L. Vander Elst, R. N. Muller, S. Lecommandoux, J. Thévenot, C. Bonduelle, A. Trotier, P. Massot, S. Miraux, O. Sandre, S. Laurent, *Nanoscale* **2015**, *7*, 3754.
[71] J. Sherwood, K. Lovas, M. Rich, Q. Yin, K. Lackey, M. S. Bolding, Y. Bao, *Nanoscale* **2016**, *8*, 17506.
[72] L. Sandiford, A. Phinikaridou, A. Protti, L. K. Meszaros, X. Cui, Y. Yan, G. Frodsham, P. A. Williamson, N. Gaddum, R. M. Botnar, P. J. Blower, M. A. Green, R. T. de Rosales, *ACS Nano* **2013**, *7*, 500.
[73] R. Chen, D. Ling, L. Zhao, S. Wang, Y. Liu, R. Bai, S. Baik, Y. Zhao, C. Chen, T. Hyeon, *ACS Nano* **2015**, *9*, 12425.
[74] H. Fu, C. Miao, Y. Rui, F. Hu, M. Shen, H. Xu, C. Zhang, Y. Dong, W. Wang, H. Gu, Y. Duan, *Biomaterials* **2019**, *222*, 119442.
[75] N. Chan, M. Laprise-Pelletier, P. Chevallier, A. Bianchi, M. A. Fortin, J. K. Oh, *Biomacromolecules* **2014**, *15*, 2146.
[76] J. Huang, L. Wang, X. Zhong, Y. Li, L. Yang, H. Mao, *J. Mater. Chem. B* **2014**, 5344.
[77] H. Groult, S. Carregal-Romero, D. Castejón, M. Azkargorta, A. B. Miguel-Coello, K. R. Pulagam, V. Gómez-Vallejo, R. Cousin, M. Muñoz-Caffarel, C. H. Lawrie, J. Llop, J. M. Piot, F. Elortza, T. Maugard, J. Ruiz-Cabello, I. Fruitier-Arnaudin, *Nanoscale* **2021**, *13*, 842.
[78] M. Xie, Z. Wang, Q. Lu, S. Nie, C. J. Butch, Y. Wang, B. Dai, *ACS Appl. Mater. Interfaces* **2020**, *12*, 53994.
[79] H. Zhou, J. Tang, J. Li, W. Li, Y. Liu, C. Chen, *Nanoscale* **2017**, *9*, 3040.
[80] K. Wang, L. Li, X. Xu, L. Lu, J. Wang, S. Wang, Y. Wang, Z. Jin, J. Z. Zhang, Y. Jiang, *ACS Appl. Mater. Interfaces* **2019**, *11*, 10452.
[81] Z. Zhou, L. Wang, X. Chi, J. Bao, L. Yang, W. Zhao, Z. Chen, X. Wang, X. Chen, J. Gao, *ACS Nano* **2013**, *7*, 3287.
[82] G. Liang, J. Han, Q. Hao, *ACS Appl Bio Mater* **2018**, *1*, 1389.
[83] Y. Luo, J. Yang, Y. Yan, J. Li, M. Shen, G. Zhang, S. Mignani, X. Shi, *Nanoscale* **2015**, *7*, 14538.
[84] Y. Chen, Q. Zhou, X. Li, F. Wang, K. Heist, R. Kuick, S. R. Owens, T. D. Wang, *Bioconjugate Chem.* **2017**, *28*, 2794.
[85] J. Sherwood, M. Rich, K. Lovas, J. Warram, M. S. Bolding, Y. Bao, *Nanoscale* **2017**, *9*, 11785.
[86] N. Zhang, Y. Wang, C. Zhang, Y. Fan, D. Li, X. Cao, J. Xia, X. Shi, R. Guo, *Theranostics* **2020**, *10*, 2791.
[87] Y. Luo, Y. Tang, T. Liu, Q. Chen, X. Zhou, N. Wang, M. Ma, Y. Cheng, H. Chen, *Chem. Commun.* **2019**, *55*, 1963.
[88] X. Wei, D. Mu, Y. Li, J. Zhao, S. Zhou, *Nano Today* **2023**, *49*, 101796.
[89] Y. Chen, M. Gao, L. Zhang, E. Ha, X. Hu, R. Zou, L. Yan, J. Hu, *Adv. Healthcare Mater.* **2021**, *10*, 2001665.
[90] Z. Shen, J. Song, Z. Zhou, B. C. Yung, M. A. Aronova, Y. Li, Y. Dai, W. Fan, Y. Liu, Z. Li, H. Ruan, R. D. Leapman, L. Lin, G. Niu, X. Chen, A. Wu, *Adv. Mater.* **2018**, 1803163.
[91] Y. Zou, D. Li, Y. Wang, Z. Ouyang, Y. Peng, H. Tomás, J. Xia, J. Rodrigues, M. Shen, X. Shi, *Bioconjug Chem* **2020**, *31*, 907.
[92] Y. Miao, H. Zhang, J. Cai, Y. Chen, H. Ma, S. Zhang, J. B. Yi, X. Liu, B.-H. Bay, Y. Guo, X. Zhou, N. Gu, H. Fan, *Nano Lett.* **2021**, *21*, 1115.
[93] Y. Li, X. Zhao, X. Liu, K. Cheng, X. Han, Y. Zhang, H. Min, G. Liu, J. Xu, J. Shi, H. Qin, H. Fan, L. Ren, G. Nie, *Adv. Mater.* **2020**, *32*, 1906799.
[94] H. Lu, A. Chen, X. Zhang, Z. Wei, R. Cao, Y. Zhu, J. Lu, Z. Wang, L. Tian, *Nat. Commun.* **2022**, *13*, 7948.
[95] X. Huang, Y. Yuan, W. Ruan, L. Liu, M. Liu, S. Chen, X. Zhou, *J. Nanobiotechnol.* **2018**, *16*, 30.
[96] D. Yoo, J.-H. Lee, T.-H. Shin, J. Cheon, *Acc. Chem. Res.* **2011**, *44*, 863.

[97] S. Suárez-García, N. Arias-Ramos, C. Frias, A. P. Candiota, C. Arús, J. Lorenzo, D. Ruiz-Molina, F. Novio, *ACS Appl. Mater. Interfaces* **2018**, *10*, 38819.

[98] X. Li, S. Lu, Z. Xiong, Y. Hu, D. Ma, W. Lou, C. Peng, M. Shen, X. Shi, *Adv. Sci.* **2019**, *6*, 1901800.

[99] J. Wang, Y. Jia, Q. Wang, Z. Liang, G. Han, Z. Wang, J. Lee, M. Zhao, F. Li, R. Bai, D. Ling, *Adv. Mater.* **2021**, *33*, 2004917.

[100] F. Li, D. Zhi, Y. Luo, J. Zhang, X. Nan, Y. Zhang, W. Zhou, B. Qiu, L. Wen, G. Liang, *Nanoscale* **2016**, *8*, 12826.

[101] L. Huang, J. Feng, W. P. Fan, W. Tang, X. X. Rong, W. J. Liao, Z. N. Wei, Y. K. Xu, A. G. Wu, X. Y. Chen, Z. Y. Shen, *Nano Lett.* **2021**, *21*, 9551.

[102] Y. D. Lu, J. Feng, Z. Y. Liang, X. Y. Lu, S. Guo, L. Huang, W. Xiong, S. J. Chen, H. M. Zhou, X. H. Ma, Y. K. Xu, X. Z. Qiu, A. G. Wu, X. Y. Chen, Z. Y. Shen, *Nanoscale Horiz.* **2022**, *7*, 403.

[103] S. Kunjachan, J. Ehling, G. Storm, F. Kiessling, T. Lammers, *Chem. Rev.* **2015**, *115*, 10907.

[104] D. Liu, Z. Zhou, X. Wang, H. Deng, L. Sun, H. Lin, F. Kang, Y. Zhang, Z. Wang, W. Yang, L. Rao, K. Yang, G. Yu, J. Du, Z. Shen, X. Chen, *Biomaterials* **2020**, *244*, 119979.

[105] Z. Y. Shen, T. X. Chen, X. H. Ma, W. Z. Ren, Z. J. Zhou, G. Z. Zhu, A. Zhang, Y. J. Liu, J. B. Song, Z. H. Li, H. M. Ruan, W. P. Fan, L. S. Lin, J. Munasinghe, X. Y. Chen, A. G. Wu, *ACS Nano* **2017**, *11*, 10992.

[106] Y. Peng, Y. Gao, C. Yang, R. Guo, X. Shi, X. Cao, *ACS Appl. Mater. Interfaces* **2021**, *13*, 27806.

[107] N. Kang, S. Son, S. Min, H. Hong, C. Kim, J. An, J. S. Kim, H. Kang, *Chem. Soc. Rev.* **2023**, *52*, 3955.

[108] T. Nakamura, C. Hipp, A. S. Dias Mourão, J. Borggräfe, M. Aldrovandi, B. Henkelmann, J. Wanninger, E. Mishima, E. Lytton, D. Emler, B. Proneth, M. Sattler, M. Conrad, *Nature* **2023**, *619*, 371.

[109] G. Lei, L. Zhuang, B. Gan, *Nat. Rev. Cancer* **2022**, *22*, 381.

[110] H. Liang, J. Guo, Y. Shi, G. Zhao, S. Sun, X. Sun, *Biomaterials* **2021**, *268*, 120530.

[111] S. Gao, H. Lin, H. Zhang, H. Yao, Y. Chen, J. Shi, *Adv. Sci.* **2019**, *6*, 1801733.

[112] Z. Shen, T. Liu, Y. Li, J. Lau, Z. Yang, W. Fan, Z. Zhou, C. Shi, C. Ke, V. I. Bregadze, S. K. Mandal, Y. Liu, Z. Li, T. Xue, G. Zhu, J. Munasinghe, G. Niu, A. Wu, X. Chen, *ACS Nano* **2018**, *12*, 11355.

[113] T. Finkel, M. Serrano, M. A. Blasco, *Nature* **2007**, *448*, 767.

[114] S. Wang, L. Yang, H. Y. Cho, S. T. Dean Chueng, H. Zhang, Q. Zhang, K. B. Lee, *Biomaterials* **2019**, *224*, 119498.

[115] Y. Zhou, S. Fan, L. Feng, X. Huang, X. Chen, *Adv. Mater.* **2021**, *33*, 2104223.

[116] C. Mao, X. Liu, Y. Zhang, G. Lei, Y. Yan, H. Lee, P. Koppula, S. Wu, L. Zhuang, B. Fang, M. V. Poyurovsky, K. Olszewski, B. Gan, *Nature* **2021**, *593*, 586.

[117] D. Li, M. Zhang, F. Xu, Y. Chen, B. Chen, Y. Chang, H. Zhong, H. Jin, Y. Huang, *Acta Pharm. Sin. B* **2018**, *8*, 74.

[118] Y. Liu, Z. Yang, X. Huang, G. Yu, S. Wang, Z. Zhou, Z. Shen, W. Fan, Y. Liu, M. Davisson, H. Kalish, G. Niu, Z. Nie, X. Chen, *ACS Nano* **2018**, *12*, 8129.

[119] D. Ling, W. Park, S. J. Park, Y. Lu, K. S. Kim, M. J. Hackett, B. H. Kim, H. Yim, Y. S. Jeon, K. Na, T. Hyeon, *J. Am. Chem. Soc.* **2014**, *136*, 5647.

[120] Z. Zhou, H. Deng, W. Yang, Z. Wang, L. Lin, J. Munasinghe, O. Jacobson, Y. Liu, L. Tang, Q. Ni, F. Kang, Y. Liu, G. Niu, R. Bai, C. Qian, J. Song, X. Chen, *Nat. Commun.* **2020**, *11*, 3032.

[121] L. Luo, M. Z. Iqbal, C. Liu, J. Xing, O. U. Akakuru, Q. Fang, Z. Li, Y. Dai, A. Li, Y. Guan, A. Wu, *Biomaterials* **2019**, *223*, 119464.

[122] S. Bai, N. Yang, X. Wang, F. Gong, Z. Dong, Y. Gong, Z. Liu, L. Cheng, *ACS Nano* **2020**, *14*, 15119.

[123] S. Lu, X. Li, J. Zhang, C. Peng, M. Shen, X. Shi, *Adv. Sci.* **2018**, *5*, 1801612.

[124] S. Fan, Y. Zhang, H. Tan, C. Xue, Y. He, X. Wei, Y. Zha, J. Niu, Y. Liu, Y. Cheng, D. Cui, *Nanoscale* **2021**, *13*, 5383.

[125] Y. Sun, H. Chen, Y. Huang, F. Xu, G. Liu, L. Ma, Z. Wang, *Biomaterials* **2021**, *274*, 120821.

Jing Yang received his B.S. degree in 2014 from Wuhan Institute of Technology and his M.S. degree in 2017 from Jinan University (Guangzhou, Guangdong) under the supervision of Prof. Mingxian Liu. He has been a Ph.D. student in Prof. Zheyu Shen's group at Southern Medical University since 2021. His current research is focused on the preparation of iron-based nanomaterials and their applications in drug delivery, MR imaging, and MR imaging-guided tumor therapy.

Yikai Xu received his master's degree from the First Military Medical University in 1989 and his Ph.D. from the Fourth Military Medical University in 1995. He has been working at the Medical Imaging Center, Nanfang Hospital, Southern Medical University since 1984. He was appointed as an associate professor in 1994 and promoted to full professor and chief physician in 2000. His research interests include immunoimaging and new contrast agents for magnetic resonance imaging.

Zheyu Shen received his Ph.D. from the Institute of Process Engineering, Chinese Academy of Sciences, under the supervision of Prof. Guanghui Ma and Prof. Toshiaki Dobashi (Gunma University, Japan). After postdoctoral studies with Prof. Kazuhiro Kohama (Gunma University, Japan) and Prof. Sheng Dai (The University of Adelaide, Australia), he was appointed an Associate Professor (2012) and promoted to Full Professor (2015) at the Ningbo Institute of Materials Technology & Engineering, Chinese Academy of Sciences. After three years as a visiting scholar at the National Institutes of Health (USA) under the supervision of Prof. Xiaoyuan Chen, he joined Southern Medical University as a Full Professor in 2019. His lab focuses on MRI contrast agents, tumor ferroptosis therapy, and immunotherapy.